JGR Space Physics

RESEARCH ARTICLE
10.1029/2021JA029224

On the Growth and Development of Non-Linear Kelvin–Helmholtz Instability at Mars: MAVEN Observations

Gangkai Poh[1,2], Jared R. Espley[2], Katariina Nykyri[3], Christopher M. Fowler[4], Xuanye Ma[3], Shaosui Xu[4], Gwen Hanley[4], Norberto Romanelli[2,5], Charles Bowers[6], Jacob Gruesbeck[2], and Gina A. DiBraccio[2]

[1]Center for Research and Exploration in Space Sciences and Technology II, Catholic University of America, Washington, DC, USA, [2]Solar System Exploration Division, NASA Goddard Space Flight Center, Greenbelt, MD, USA, [3]Department of Physical Sciences, Center for Space and Atmospheric Research, Embry-Riddle Aeronautical University, Daytona Beach, FL, USA, [4]Space Sciences Laboratory, University of California, Berkeley, Berkeley, CA, USA, [5]Center for Research and Exploration in Space Sciences and Technology II, University of Maryland Baltimore County, Baltimore, MD, USA, [6]Department of Climate and Space Sciences and Engineering, University of Michigan, Ann Arbor, MI, USA

Abstract In this study, we have analyzed Mars Atmosphere and Volatile EvolutioN (MAVEN) observations of fields and plasma signatures associated with an encounter of fully developed Kelvin–Helmholtz (K–H) vortices at the northern polar terminator along Mars' induced magnetosphere boundary. The signatures of the K–H vortices event are: (a) quasi-periodic, "bipolar-like" sawtooth magnetic field perturbations, (b) corresponding density decrease, (c) tailward enhancement of plasma velocity for both protons and heavy ions, (d) co-existence of magnetosheath and planetary plasma in the region prior to the sawtooth magnetic field signature (i.e., mixing region of the vortex structure), and (e) pressure enhancement (minimum) at the edge (center) of the sawtooth magnetic field signature. Our results strongly support the scenario for the non-linear growth of K–H instability along Mars' induced magnetosphere boundary, where a plasma flow difference between the magnetosheath and induced-magnetospheric plasma is expected. Our findings are also in good agreement with 3-dimensional local magnetohydrodynamics simulation results. MAVEN observations of protons with energies greater than 10 keV and results from the Walén analyses suggests the possibility of particle energization within the mixing region of the K–H vortex structure via magnetic reconnection, secondary instabilities or other turbulent processes. We estimate the lower limit on the K–H instability linear growth rate to be $\sim 5.84 \times 10^{-3}$ s^{-1}. For these vortices, we estimate the instantaneous atmospheric ion escape flux due to the detachment of plasma clouds during the late non-linear stage of K–H instability to be $\sim 5.90 \times 10^{26}$ particles/s. Extrapolation of loss rates integrated across time and space will require further work.

Key Points:

- Mars Atmosphere and Volatile EvolutioN (MAVEN) observed magnetic field and plasma signatures consistent with the encounter of fully developed Kelvin–Helmholtz (K–H) vortices along Mars' induced magnetospheric boundary (IMB)
- Close agreement between 3-D magnetohydrodynamics simulation result and MAVEN observation support the scenario for K–H instability occurrence along Mars' IMB
- We estimated the instantaneous atmospheric ion escape flux due to detachment of plasma clouds from K–H instability to be $\sim 5.9 \times 10^{26}$ s^{-1}

Supporting Information:

Supporting Information may be found in the online version of this article.

Correspondence to:

G. Poh,
gangkai.poh@nasa.gov

Citation:

Poh, G., Espley, J. R., Nykyri, K., Fowler, C. M., Ma, X., Xu, S., et al. (2021). On the growth and development of non-linear Kelvin–Helmholtz instability at Mars: MAVEN observations. *Journal of Geophysical Research: Space Physics*, *126*, e2021JA029224. https://doi.org/10.1029/2021JA029224

Received 6 FEB 2021
Accepted 27 JUL 2021

1. Introduction

In the absence of a global intrinsic magnetic field, Mars' upper atmosphere and ionosphere are constantly eroded by processes occurring through direct interaction with the solar wind. This solar wind-planetary interaction is complicated by the presence of crustal magnetic fields, which are scattered across the planet's surface, with the strongest sources located in the Southern Hemisphere (Acuna et al., 1999; Connerney et al., 2015). The intensity of these southern crustal fields are strong enough to standoff the solar wind, forming what are known as "mini-magnetospheres" (e.g., Mitchell et al., 2001). Understanding the dynamics of the Martian system in order to establish the physical (and chemical) processes contributing to atmospheric loss to space is a main objective of the Mars Atmosphere and Volatile EvolutioN (MAVEN) mission (Jakosky et al., 2015). It was believed that the dominant atmospheric loss mechanism is due to solar wind pick-up and acceleration of planetary ions by the convection electric field resulting from the draping of the interplanetary magnetic field (IMF) as solar wind encounters a non-magnetized planet (e.g., Barabash et al., 2007; Halekas et al., 2016), although it is thought that photochemical escape played a more important role in the current epoch (Jakosky et al., 2018). Kelvin–Helmholtz (K–H) instability, which can form along the boundary between the solar wind and Martian environment, may also contribute to this escape. However, the significance of K–H instability in the overall plasma escape of the Martian ionosphere is rarely discussed and explored.

The K–H instability is a fundamental plasma process in many astrophysical plasma environments. Its development and growth is known to occur along the interface of two fluids in the presence of a velocity shear. As such, K–H instability is commonly observed along the flanks of globally magnetized planets, such as Mercury (Boardsen et al., 2010; Gershman et al., 2015; Liljeblad et al., 2015; Sundberg et al., 2012), Earth (see review by Masson and Nykyri [2018] and references therein) and Saturn (e.g., Delamere et al., 2013; Masters et al., 2009). In this region, the K–H instability is driven by a velocity flow shear between the shocked solar wind in the magnetosheath and magnetospheric plasma. Theoretical studies of the K–H instability at Earth using resistive magnetohydrodynamics (MHD) (e.g., Ma et al., 2017; Nykyri & Otto, 2001), Hall-MHD (e.g., Ma et al., 2019; Nykyri & Otto, 2004), hybrid (e.g., Cowee et al., 2009; Delamere et al., 2013; Fujimoto & Terasawa, 1994; Nakamura et al., 2004), and particle-in-cell (e.g., Nakamura et al., 2017) numerical simulations have been conducted extensively to understand the instability criteria, development and role in transporting mass, energy and momentum across plasma boundary layers during its non-linear stage. In an ideal, incompressible MHD plasma, the instability criterion for K–H instability to occur is given by the relation (Chandrasekhar, 1961):

$$\left[\boldsymbol{k}\cdot\left(\mathbf{v}_1-\mathbf{v}_2\right)\right]^2 > \frac{n_1+n_2}{\mu_0 m_i n_1 n_2}\left[\left(\boldsymbol{k}\cdot\mathbf{B}_1\right)^2+\left(\boldsymbol{k}\cdot\mathbf{B}_2\right)^2\right] \quad (1)$$

where $\mathbf{v}$, n, m_i, and $\mathbf{B}$ represents the plasma flow velocity, number density, ion mass and magnetic field, respectively; the subscript indices (1 and 2) denote the two plasma regions across the flow shear boundary and $\boldsymbol{k}$ represents the propagation direction of the K–H waves tangential to the flow shear plane. The analytical expression of the instability criterion shows that a minimum plasma flow shear is required for the boundary layer to be unstable to K–H instability, while the magnetic tension force resulting from transverse magnetic field (i.e., magnetic field along $\boldsymbol{k}$) and/or plasma density gradient across the shear boundary can suppress (i.e., stabilizing effect) the growth of K–H waves. Once the instability condition is satisfied, a small perturbation can cause the boundary to be unstable and grow as surface waves at the K–H unstable flow shear boundary in its linear stage. These linear waves can evolve into large-scale, rolled-up K–H vortices during the non-linear stage when the growth is no longer constant, allowing for mixing and transport of plasma across the boundary within the full-developed vortices via localized magnetic reconnection of the twisted magnetic field structure (Nakamura & Fujimoto, 2005; Nykyri & Otto, 2001, 2004; Otto & Fairfield, 2000), turbulence (Matsumoto & Hoshino, 2004), secondary instabilities (e.g., Cowee et al., 2009; Faganello et al., 2008; Matsumoto & Hoshino, 2006; Nakamura & Daughton, 2014), and finite gyroradius effects (Fujimoto & Terasawa, 1994; Terasawa et al., 1992) within or along the boundaries of the vortices.

Three-dimensional simulation and theoretical studies of the K–H instability (e.g., Borgogno et al., 2015; Fadanelli et al., 2018; Faganello et al., 2012; Ma et al., 2017; Sisti et al., 2019) have also identified another type of vortex-induced reconnection process in the mid-latitude region along the magnetopause, especially in the case where an in-plane magnetic field component is present. In this scenario, the "twisting" of the magnetic field lines along the in-plane direction due to the vortex motion can facilitate the occurrence of magnetic reconnection at higher latitude along the in-plane direction away from the equatorial plane where the K–H vortices were formed. The complex magnetic field geometry arising from the double mid-latitude reconnection could result in the formation of magnetic flux ropes (instead of magnetic islands in the quasi-2-D picture of the K–H instability). Such vortex-induced reconnection process no longer spatially limit the transport of plasma across the flow shear boundaries to the low-latitude region and had been reported in multiple observational studies (e.g., Bavassano et al., 2010; Faganello et al., 2014; Vernisse et al., 2020).

Observations of K–H vortices at Earth (e.g., Eriksson et al., 2016; Fairfield et al., 2000; Hasegawa et al., 2004, 2006; Kavosi & Raeder, 2015; Nykyri et al., 2006) are generally characterized by quasi-periodic, sawtooth-like (i.e., sudden changes preceded by slow recovery) wave fluctuations in the magnetic field measurements, and similar periodic wave patterns in all plasma quantities (i.e., density, temperature, and velocity). All of the observed signatures were thought to be a result of the spacecraft crossing of the sharp shear boundary at the trailing edge (or spine) of the vortex from the mixing region at the leading edge of the vortex to the magnetosheath (Fairfield et al., 2000, 2007; Sundberg et al., 2011). The reader is referred to Figure 2 of Sundberg et al. (2010) for illustration on the interpretation of the two waveforms during linear and non-linear stages of the K–H instability. The co-existence of the cold magnetosheath and hot magnetospheric plasma population within the mixing region of the vortex, where plasma can be transported across the flow shear

boundary, is also indicative of the formation of K–H vortices associated with the development of non-linear K–H instability (Hasegawa et al., 2004). The centrifugal motion of the vortex requires the tenuous magnetospheric plasma within the mixing region to be accelerated to speeds faster than the denser magnetosheath plasma to maintain radial force balance (Takagi et al., 2006). As such, the presence of low-density magnetospheric plasma with speed faster than magnetosheath can be used as identification feature for fully developed K–H vortices using single-spacecraft measurements (Hasegawa et al., 2006; Kavosi & Raeder, 2015).

It is important to note that the sawtooth magnetic field signature of a fully developed K–H vortex structure resembles the characteristic bipolar signature associated with magnetic flux ropes, which are helical flux tubes with strong axial core fields commonly observed in many regions of intrinsic and induced planetary magnetospheres (e.g., magnetopause and magnetotail), and interplanetary space (e.g., coronal mass ejections) (see review by Eastwood and Kiehas [2015]). This could easily lead to misidentification between the two fundamentally different magnetic structures. However, both K–H vortex and flux ropes do have significant differences and one of them is the presence of a strong magnetic field enhancement associated with the core field along the axis of the flux rope, which coincides with the center or inflection point of the bipolar signature (see Figure 2 in DiBraccio et al. [2015] for illustration). Such a signature is typically absent in a K–H vortex since the sawtooth signature is associated with the crossing of a quasi-planar boundary layer. Furthermore, due to the centrifugal motion within the vortex "pushing" the plasma radially outwards, the maximum (minimum) total pressure (i.e., sum of thermal plasma pressure for each ion species and magnetic pressure) is expected at the edge (center) of the vortex while a maximum total pressure is typically observed at the center of the flux rope instead.

The K–H instability has also been thought to occur in the plasma environments of unmagnetized planets such as Venus and Mars. Unlike Earth and other magnetized planets, the Venusian, and Martian ionosphere interacts directly with the solar wind due to the lack of an intrinsic planetary magnetic field, resulting in velocity shear along the boundary separating the magnetosheath and ionosphere where K–H instability could potentially develop. Theoretical studies on K–H instability at Venus (Elphic & Ershkovich, 1984; Wolff et al., 1980) concluded that K–H instability can form along the Venusian ionopause with a short growth time of ∼0.5 to a few seconds. Numerical simulations (e.g., Amerstorfer et al., 2010; Möstl et al., 2011; Terada et al., 2002; Thomas & Winske, 1991) also demonstrated that the K–H waves formed along the ionopause can grow, steepened into vortices structures during the non-linear stage, and subsequently detached from the ionosphere in the form of ionospheric "bubbles" (or plasma clouds) due to turbulence within vortex structure. These plasma clouds are eventually convected downtail with the solar wind, contributing to atmospheric loss. Observations of vortex structures associated with K–H instability and detached plasma clouds were reported by Brace et al. (1982), and subsequently Pope et al. (2009) using Pioneer Venus Orbiter measurements. More recently, statistical analysis of ionospheric boundary waves associated with K–H instability conducted by Chong et al. (2018) using Venus Express observations suggest that the draping of magnetic field lines plays an important role in the formation of K–H instability at Venus by enhancing the plasma flow, and consequently the velocity shear, along the dawn-dusk direction.

The interaction between the solar wind and Mars' plasma environment, on the other hand, is unique and different than Venus due to the presence of strong Martian remnant crustal field with the strongest intensity mainly in the Southern Hemisphere at ∼180°E longitude (e.g., Connerney et al., 2015). Mars' crustal magnetic field intensity is strong enough to create a magnetic barrier against the solar wind, thereby creating a hybrid magnetosphere which consist of a (to first order) miniature Earth-like dipole field in the Southern Hemisphere surrounded by induced and draped field (DiBraccio et al., 2018; Dubinin et al., 1994; Xu et al., 2020). The presence of the crustal magnetic field further complicates the magnetic field topology (i.e., open, closed and draped field lines) and dynamics within the Martian plasma environment (Brain et al., 2007; Lillis & Brain, 2013; Xu et al., 2017, 2018, 2019, 2020; Weber et al., 2020). As such, it becomes more relevant and important to ask the following question: where is the K–H unstable flow shear boundary at Mars?

Penz et al. (2004) investigated the occurrence of K–H instability at Mars using an analytical approach to solve the MHD equations in the IMF coordinate system. By calculating the instability growth rates for different magnetosheath flow velocity and plasma density, and comparing it to the magnetic barrier formation time, Penz et al. (2004) found that the terminator plane is conducive for the non-linear development of K–H

instability, though preferably at the equatorial terminator flanks. They also estimated an escape rate of O^+ ions from the detached plasma clouds associated with K–H instability on the order of 10^{23}–10^{24} s^{-1}, which is comparable to other non-thermal loss processes. Gunell et al. (2008) reported observations of oscillations in electron density, ion (O^+ and CO_2^+) density and ion velocity, and suggested K–H instability as likely cause of these oscillations. More recently, Ruhunusiri et al. (2016) reported observations of partially developed K–H vortices using magnetic field and plasma measurements collected from MAVEN. They further suggested the possibility of these partially developed K–H vortices being fully developed further downstream.

Despite previous attempts by earlier studies to apply our understanding of K–H instability at Venus to the Martian plasma environment, the excitation and evolution of K–H instability at Mars, and its contribution to the overall ionospheric escape remains largely unexplored and poorly understood. This can be attributed to difficulties in observing fully developed vortices associated with K–H instability and the lack of simultaneous in-situ magnetic field and plasma measurements before MAVEN. Although it is not the first spacecraft to observe and examine K–H instability in unmagnetized planets, the MAVEN spacecraft contains a comprehensive suite of instruments suited to further our physical understanding of K–H instability at Mars.

In this study, we present a case study on MAVEN's observation of large-amplitude, quasi-periodic sawtooth-like magnetic field oscillations, with corresponding variations of plasma density and velocity. Analysis of the magnetic field and plasma measurements collected by MAVEN shows that the observed quasi-periodic signatures are consistent with the observations of fully developed, rolled-up vortices and plasma mixing within the vortex structure associated with the non-linear stage of K–H instability. Our analysis results further suggest the possibility of magnetic reconnection occurring within the K–H vortices. We also present 3-D local MHD simulation results of K–H instability using magnetosheath and induced magnetospheric magnetic field and plasma conditions observed by MAVEN as initial conditions. We estimated the planetary heavy ion escape flux from detached plasma clouds during the later stage of the K–H instability, and compared our calculation with escape rates estimated from earlier studies of other non-thermal loss processes and numerical simulation.

2. MAVEN Observation: April 16, 2017 Event

In this study, we use the magnetic field and plasma measurements collected by the MAVEN spacecraft. The Magnetometer (MAG, Connerney et al., 2015) measures the magnetic field at sampling rates of 32 vectors/s. The SupraThermal And Thermal Ion Composition (STATIC, McFadden et al., 2015) and the Solar Wind Electron Analyzer (SWEA, Mitchell et al., 2016) instrument provides the energy spectrogram, velocity distribution and moments of H^+ and heavy ions (i.e., O^+ and O_2^+), and moments of electrons at time resolution of 4 and 2s, respectively. In this study, full-resolution measurements from MAG, STATIC and SWEA are utilized to identify the characteristic magnetic fields and plasma signatures associated with the encounter of K–H vortices. The MAG and STATIC observations are also used together in the minimum variance and Walen analyses, and comparison with results from 3-D MHD simulation to further enhance the scientific returns of single-spacecraft measurements. The coordinate system used in our analyses presented in this study is the Mars Solar Orbital (MSO) coordinate system, where X_{MSO} axis points sunward along the Sun – Mars line, Y_{MSO} axis points in the direction opposite to Mars' orbital velocity, and Z_{MSO} axis completes the right-handed coordinate system.

2.1. Magnetic Fields and Plasma Signatures of Kelvin–Helmholtz Vortices

Figure 1a shows the MAVEN orbit projected on the (*left*) equatorial (i.e., *XY*-) and (*right*) cylindrical (i.e., *Xρ*-) plane, where $\rho = \sqrt{Y^2 + Z^2}$, on April 16, 2017. The red line represents MAVEN's trajectory when the spacecraft observed the quasi-periodic sawtooth-like magnetic field oscillations associated with K–H instability. The purple and blue dashed lines represent the location of Mars' empirical bow shock (BS) and induced magnetospheric boundary (IMB) (Vignes et al., 2000), respectively. In this study, the IMB (also synonymously referred to as the magnetic pileup boundary or MPB [Crider et al., 2000; Matsunaga et al., 2017; Winterhalter et al., 2004]) is defined as the boundary that separates the magnetosheath and the inner induced magnetosphere (Bertucci et al., 2011; Espley, 2018). Figure 1a shows that MAVEN encounter the quasi-periodic sawtooth magnetic field signatures near the polar terminator at high solar zenith angle

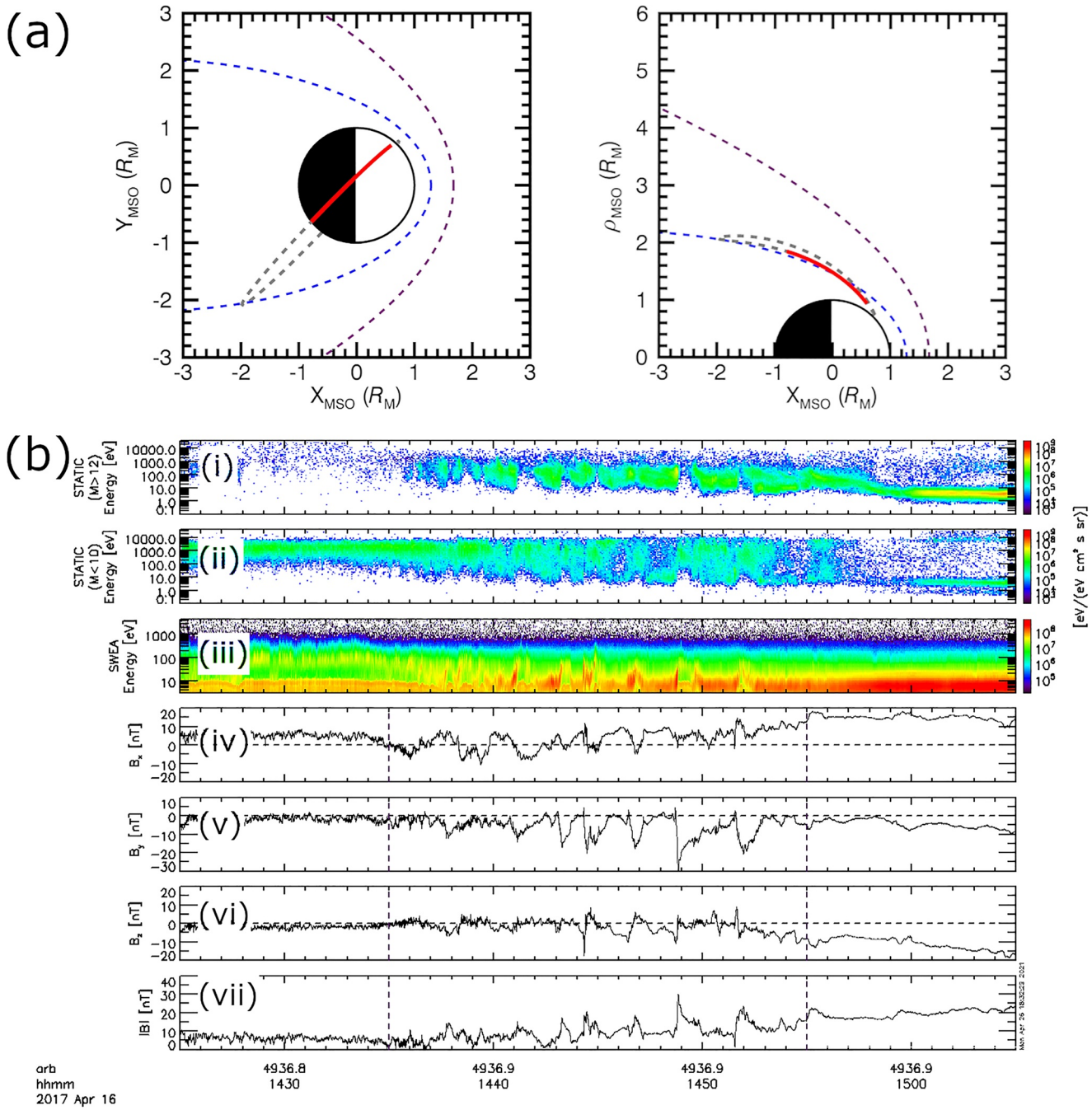

Figure 1. (a) MAVEN orbit (gray dashed lines) on April 16, 2017 in the equatorial *xy*-plane (left) and cylindrical plane (right). Purple and blue dashed lines show the typical location for the bow shock and induced magnetosphere boundary (Vignes et al., 2000), respectively. The MAVEN spacecraft trajectory is shown by the red line. (b) Magnetic field and plasma measurements observed by MAVEN on April 16, 2017. Panels (i and ii): Energy spectrograms observed by STATIC for heavy (i.e., atomic mass > 12) and lighter (i.e., atomic mass < 10) ions, respectively. Panel (iii): Electron energy spectrograms observed by SWEA. Panels (iv–vii): *x*, *y*, and *z*-components, and magnitude of the magnetic field measurements. This figure shows that MAVEN observed these quasi-periodic sawtooth-like magnetic field oscillations with corresponding perturbation patterns in the plasma measurements at the northern polar terminator along the induced magnetospheric boundary.

(SZA) in the Northern Hemisphere. Note that the spacecraft "skimmed" along the induced magnetosphere boundary as it travels from the magnetosheath into the inner induced magnetosphere, thereby allowing for the observation of the boundary surface over a wide range of SZA.

Panels (i and ii) of Figure 1b shows the energy spectrogram for ions with mass >12 amu (i.e., O^+ and O_2^+) and mass <10 amu (i.e., H^+ and He^+) measured by STATIC, respectively; Note that O^+ and O_2^+, and H^+ and He^+ are the dominant ions in these respective mass ranges. Panel (iii) shows the electron energy spectrogram measured by SWEA. The *x*, *y*, and *z*-components, and magnitude (|**B**|) of the magnetic field measured by MAG are shown in Panels (iv–vii), respectively. The interval starts with MAVEN in the magnetosheath as shown by the weak and highly turbulent (i.e., high level of fluctuations) |**B**|, lack of planetary heavy ions, and presence of protons with broad ranges of energy between 100 eV and 10 keV consistent with shocked solar wind. Between 14:35:00 and 14:55:00 UTC, MAVEN encountered the induced magnetosphere boundary as shown by the steady increase in |**B**|. The spacecraft subsequently entered the inner induced magnetosphere (sometimes called the magnetic pileup region) at ∼14:55 UT, which is characterized by the strong |**B**| at ∼20 nT with minimum fluctuations, and the presence of cold (i.e., <10 eV) protons, heavy ions and electrons of planetary origins. During the traversal of the Martian induced magnetosphere boundary, MAVEN observed multiple quasi-periodic sawtooth-like signatures in all components of the magnetic field. Both STATIC and SWEA also observed corresponding variations in the fluxes and energies of protons, heavy ions and electrons corresponding to the sawtooth magnetic field signatures.

A subset of these magnetic field and plasma observations are shown over a 20-min interval in Figure 2. This interval includes the period when MAVEN crossed the induced magnetosphere boundary characterized by the (a) increase in |**B**| from ∼5 to 15 nT, (b) decrease in high-frequency fluctuation of |**B**|, (c) gradual increase in B_X due to the draping of the IMF lines, (d) increase in heavy planetary ions density from ∼0.01 to 10 cm^{-3}, and (e) decrease (increase) of electron temperature (density). Interestingly, MAVEN also observed a constant proton density of ∼0.8 cm^{-3} across the boundary, which is not unexpected at high SZA as shown by a recent statistical study of the proton density distribution in the Martian magnetosheath (see Figure 2 in Wang et al. [2020]). MAVEN further observed a decrease in the tailward (i.e., negative *x*-direction) H^+ flow velocity (blue line, Panel [f] in Figure 2) from ∼−350 to −10 km/s as the spacecraft entered the induced magnetosphere proper; similar decreases in tailward O^+ and O_2^+ flow (blue line, Panel [h and i] in Figure 2) were also observed. The observation of a strong gradient in the tailward plasma flow velocity across the boundary between the magnetosheath and induced magnetosphere indicates that the induced magnetosphere boundary can be unstable to K–H instability. MAVEN further observed quasi-periodic "sawtooth-like" oscillations in both magnetic field and plasma measurements in addition to the overall changes associated with the crossing of the induced magnetosphere boundary. Note that the start of each perturbations is delineated by gray dashed lines for visual guidance. Panel (a) shows sawtooth wave pattern perturbations (at ∼14:37:25, 14:40:43, 14:43:00, 14:44:19, 14:46:29, 14:48:35, and 14:51:30 UTC) in all components of the measured magnetic field vectors with periodicity of ∼1–3 min. Each wave cycle generally starts with a sudden anti-correlated change in the magnitude and polarity of the *x*- and *z*-component (i.e., B_X and B_Z) of the magnetic field, where the maxima of B_z coincides with the minima of B_X and vice versa. The perturbations in B_X and B_Z are often accompanied by an abrupt increase in the magnitude of the *y*-component of the magnetic field vector (i.e., B_Y) of ∼10–30 nT, followed by a gradual return to background magnetic field values to create a series of quasi-periodic sawtooth pattern in the magnetic field. The stark similarity between the unique sawtooth magnetic field perturbation pattern observed by MAVEN and known magnetic field characteristics of fully developed K–H vortices observed at Earth (e.g., Fairfield et al., 2000) and other planets (e.g., Mercury [Liljeblad et al., 2015; Sundberg et al., 2012]) strongly suggest that the spacecraft encounters a wave train of K–H vortices associated with K–H instability occurring along the observed flow shear boundary layer between the magnetosheath and induced magnetosphere.

Furthermore, the periodic perturbation patterns in B_X and B_Z are consistent with expected signatures of K–H waves observed near the polar terminator region and tailward flow gradient in the *xz*-plane. Note that the magnitude of B_Y often (but not always) exhibit the largest perturbations, which is not uncommon due to the presence of a strong out-of-plane (i.e., *y*-direction) background magnetic field and the twisting of magnetic field lines within the K–H vortices. We would like to point out that our observation is also consistent with the development of K–H instability during its non-linear stage for this time interval. The observation of

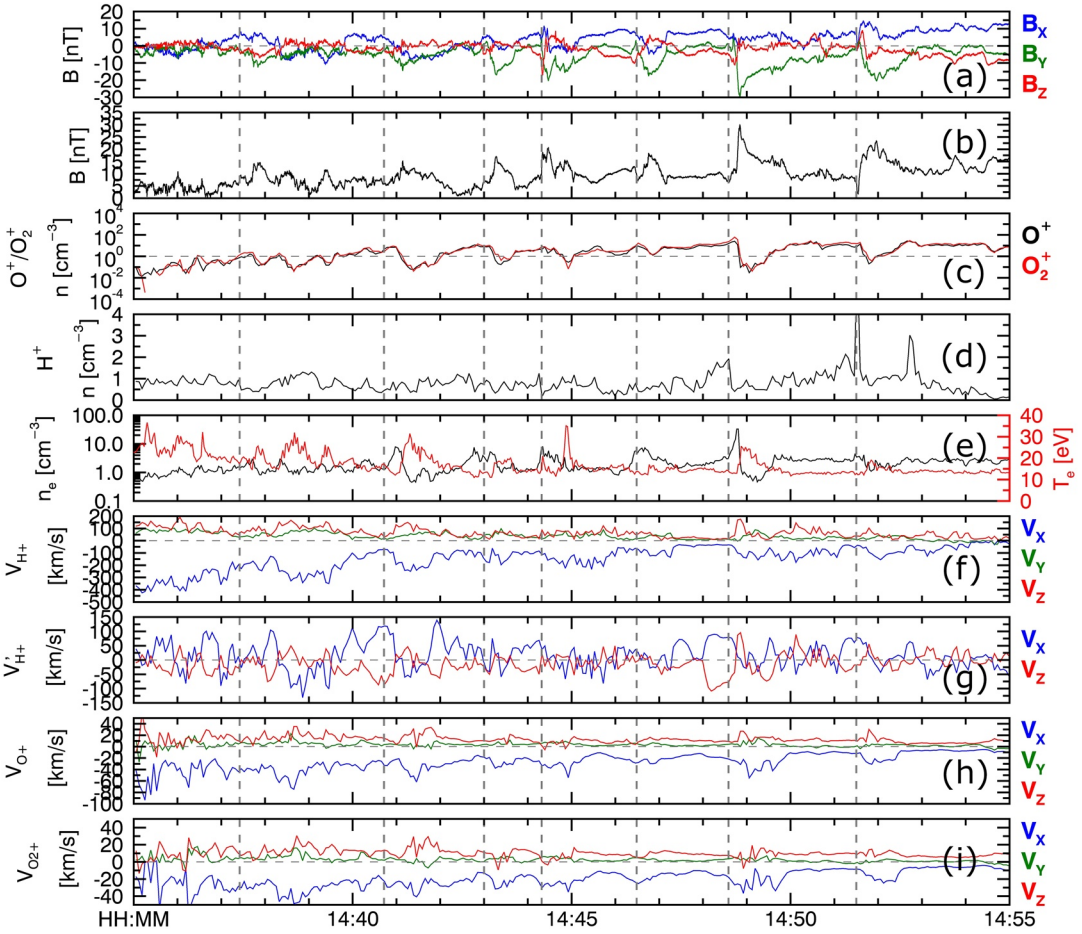

Figure 2. The closed-up 20-min interval of magnetic field, and electrons and ions (H^+, O^+, and O_2^+) measurements (i.e., density, temperature and velocity) observed by MAVEN on April 16, 2017. Panels (a and b): *x*, *y*, and *z*-components and magnitude of the magnetic field vectors. Panels (c–e): Plasma density of heavy ions and H^+, and the electron density and temperature computed from STATIC and SWEA measurements, respectively. Panels (f, h, and i): H^+, O^+, and O_2^+ plasma velocity. Panel (g): H^+ plasma velocity in the HT frame. Vertical gray dashed lines mark the start of the magnetic field and plasma perturbations associated with each K–H wave cycle. This figure shows that the quasi-periodic sawtooth-like magnetic field oscillations and corresponding plasma velocity perturbations of H^+, O^+, and O_2^+ are associated with the encounter of fully developed K–H vortices formed during the non-linear stage of the K–H instability.

only one outbound crossing of the boundary layer (i.e., abrupt change in magnetic field), or the vortex spine, followed by the mixing region of the consecutive vortex (i.e., gradual transition to background magnetic field values) indicates the formation of a vortex structure. The reader is referred to Figure 2 in Sundberg et al. (2010) for illustration and further explanation of expected magnetic field signatures consistent with observation of a well-developed K–H vortex. The linear surface waves initiated during the initial stage of the K–H instability lacks the sawtooth-like magnetic field signature due to an absence of a mixing region and steepening of the wave at the leading and trailing edge of the wave, respectively. Instead they are characterized by a series of well-defined periodic pair of inbound and outbound crossings of the boundary layer (Sundberg et al., 2010) between the two flow regions. Hence, the unique sawtooth magnetic field signature observed in this study supports the idea of K–H vortices formation along the Martian induced magnetosphere boundary during the non-linear stage of the K–H instability.

The possible explanation of the quasi-periodic sawtooth magnetic field perturbation pattern as fully developed K–H vortices is further supported by similar correlated perturbations in the plasma measurements. Panels (c and e) show simultaneous observations of multiple quasi-periodic sudden decreases in heavy planetary ions (O^+ and O_2^+) and electron densities, and increase in electron temperature that coincides with the observed sawtooth magnetic field signatures, followed by a slow return to the background values; the proton density displayed in Panel (d) shows a similar but weaker perturbation pattern, although such varia-

tions in the proton density are not always observed. The observed perturbations in ions and electron densities support our magnetic field observations that MAVEN crosses the boundary separating the induced magnetosphere, which contains higher densities of heavy ions and colder electrons, and the magnetosheath. The slow recovery that followed suggests the presence of a transition region where plasma population from the two regions co-exist.

The proton velocity displayed in Panel (f) shows periods of enhanced plasma flows most notably in the tailward (or negative *x*-) direction, and also in the positive *z*-direction corresponding to the observations of the sawtooth magnetic field perturbations. Our observation of the proton velocity is consistent with the expected enhanced flow directions due to vortex-induced centrifugal motion in the upper portion of the vortex structure. Similar but smaller flow enhancements in the *x*–*z* direction were also observed for the heavy ions as shown in Panels (h and i) likely due to mass loading within the vortex structure and its surrounding. The observed positive enhancement proton velocity in the *y*-direction also suggest the presence of a net duskward (i.e., positive *y*-direction in the MSO coordinate system) current density in the direction normal to the flow shear plane, possibly due to the twisting of magnetic field lines in the vortex (Masters et al., 2010; Ruhunusiri et al., 2016). Another characteristic observations of K–H vortices during their non-linear phases (e.g., Eriksson et al., 2016; Faganello et al., 2014; Hasegawa et al., 2004) is the "bipolar" pattern of the plasma velocity component perpendicular to the unperturbed boundary. The expected bipolar plasma flow pattern within a vortex structure can be observed in a steady-state plasma configuration or a frame in which the convective electric field vanishes (i.e., the deHoffman–Teller frame [Sonnerup et al., 1987]) and by Faraday's law, the structure is stationary. The determination and analysis of the deHoffman–Teller (HT) frame will be discussed further in later sections of this study. However, as shown in Panel (g) of Figure 2 in this section, plasma flow reversal in the *x*- and *z*-direction (where $\mathbf{V}'_{H+} = \mathbf{V}_{H+} - \mathbf{V}_{HT}$) was observed in a quasi-steady-state HT frame as the spacecraft traverses the train of K–H vortices, thereby further supporting the scenario that MAVEN observed a train of fully developed vortices associated with the non-linear development of K–H instability along the induced magnetosphere boundary. Note that the bipolar pattern of the plasma flow might not be clearly identifiable for some events in this interval possibly due to the fact that the K–H vortices have been strongly perturbed by secondary instabilities or magnetic reconnection.

The presence of these "faster-than-magnetosheath" low-density plasma flows is one of the many criteria used to identify fully rolled-up K–H vortices observed at Earth and is thought to be caused by centrifugal effects within the vortex, where the tenuous magnetospheric plasma must rotate faster than the denser magnetosheath plasma to maintain radial force balance (Takagi et al., 2006). This plasma flow signature is typically (but not always) observed in the scatterplot of the *x*-component of the flow velocity (i.e., V_X) versus proton density (Hasegawa et al., 2006; Kavosi & Raeder, 2015) and the absence of such signature had been used in the identification of partially developed K–H vortices at Mars (Ruhunusiri et al., 2016). However, it should be noted that the "faster-than-magnetosheath" signature can only be observed in cases when there is a significant density gradient across the boundary (Hasegawa et al., 2006; Takagi et al., 2006). Furthermore, Cowee et al. (2009, 2010) demonstrated that the high-speed, low-density flow signature may not form in cases of uniform density across the flow shear layer. This is similar to the case study presented here, where an overall constant proton density across the boundary was observed as shown in Panel (d) of Figure 2. Therefore, the use of the "faster-than-magnetosheath" identification criteria for K–H vortices is not applicable for our study.

2.2. Kelvin–Helmholtz Waves Versus Magnetic Flux Ropes

We also examined each wave cycle in detail to demonstrate that observed signatures are indeed consistent with K–H vortices instead of magnetic flux ropes. Figure 3a shows the close-up interval of a wave cycle example. The schematic illustration displayed in top panel of Figure 3a shows the interpretation of a K–H wave cycle delineated by two vertical dashed lines, which also marks the center of the sawtooth magnetic field signature associated with the outbound crossing of the boundary layer. Panels (i–iii) shows the magnetic field components and magnitude of the magnetic field, and heavy ion densities, respectively. Panel (iv) shows the thermal plasma pressure for each ion species (i.e., H^+, O^+, and O_2^+), while Panel (v) shows the total thermal pressure, magnetic pressure and total pressure. It is evident that the "bipolar-like" sawtooth magnetic field signatures observed at ~14:48:46 and ~14:51:45 UTC displayed in Panels (i and ii)

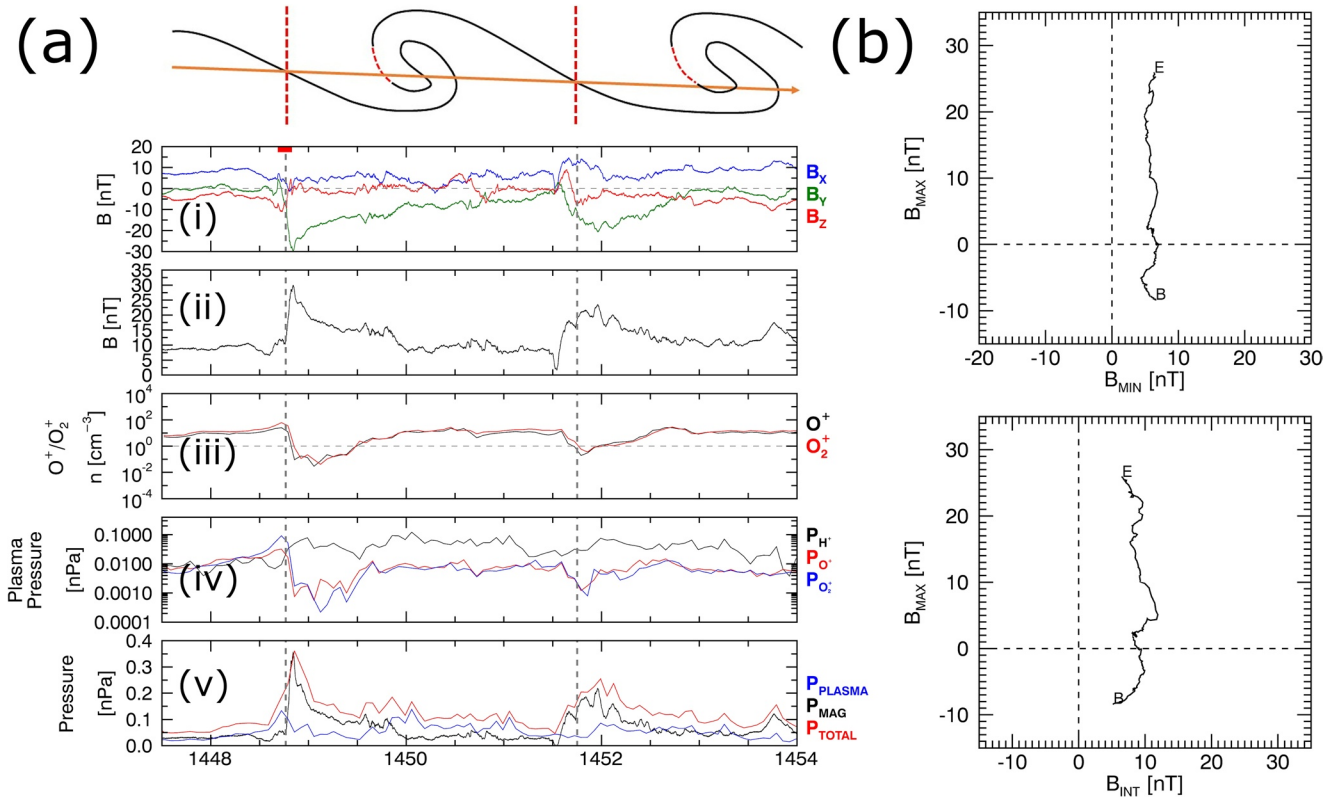

Figure 3. (a) Top: Schematic illustration of a K–H wave cycle example between 14:49:30 to 14:54:00 UTC, interpreted based on the magnetic field and plasma measurements. Orange arrow shows MAVEN's possible trajectory through the wave cycle. Panels (i and ii): Components and magnitude of the magnetic field measurements observed by MAG. Panel (iii): Plasma density of heavy ions (O^+ and O_2^+) measured by the STATIC instrument. Panels (iv and v): Plasma pressures for each ion species and total pressure (i.e., sum of the magnetic pressures and total plasma pressure for all ion species). (b) MVA hodogram of the boundary crossing marked by the red bar in Panel (i) of Panel (a). Analysis of individual saw-tooth-like magnetic field signature indicates that these signatures are consistent with the observations of K–H vortices, instead of flux ropes.

show neither a clear strong enhancement in the magnetic field components (commonly associated with the core field of the flux rope) nor maximum in magnetic field intensity that aligns with the center of the saw-tooth signature (gray dashed lines). We also performed the minimum variance analysis (MVA) technique (Sonnerup & Scheible, 1998) on the sawtooth signature observed at 14:48:46 UTC (red bar). The MVA hodograms displayed in Figure 3b shows little or no magnetic field variation in the minimum (B_{min}) and intermediate (B_{int}) variance direction, which are signatures typically representative of a boundary (or current sheet) layer crossing, instead of a flux rope's. Not shown here, the MVA hodograms for the sawtooth signature at 14:51:45 UTC are also consistent with a boundary layer crossing.

Furthermore, Panel (v) shows an increase in total pressure (red line) around ~14:49:45 UTC just as the spacecraft went from the magnetosheath into the "induced magnetosphere-like" region as shown by the simultaneous increase in O^+ and O_2^+ densities. The observed maxima in total pressure, which is followed by an extended time period of lower total pressure, is consistent with signatures expected during the encounter of the leading edge of the vortex since total pressure is expected to increase at the edge of the vortex structure due to centrifugal effect as mentioned earlier. All of the observations and analysis results outlined in this section strongly support the scenario where MAVEN crosses the first boundary layer at 14:48:46 UTC, followed by the encounter of a K–H vortex before exiting the second boundary layer at 14:51:45 UTC into the trailing region of the vortex as illustrated in Figure 3a, and that the observed sawtooth signatures are unlikely to be associated with the encounter of magnetic flux ropes.

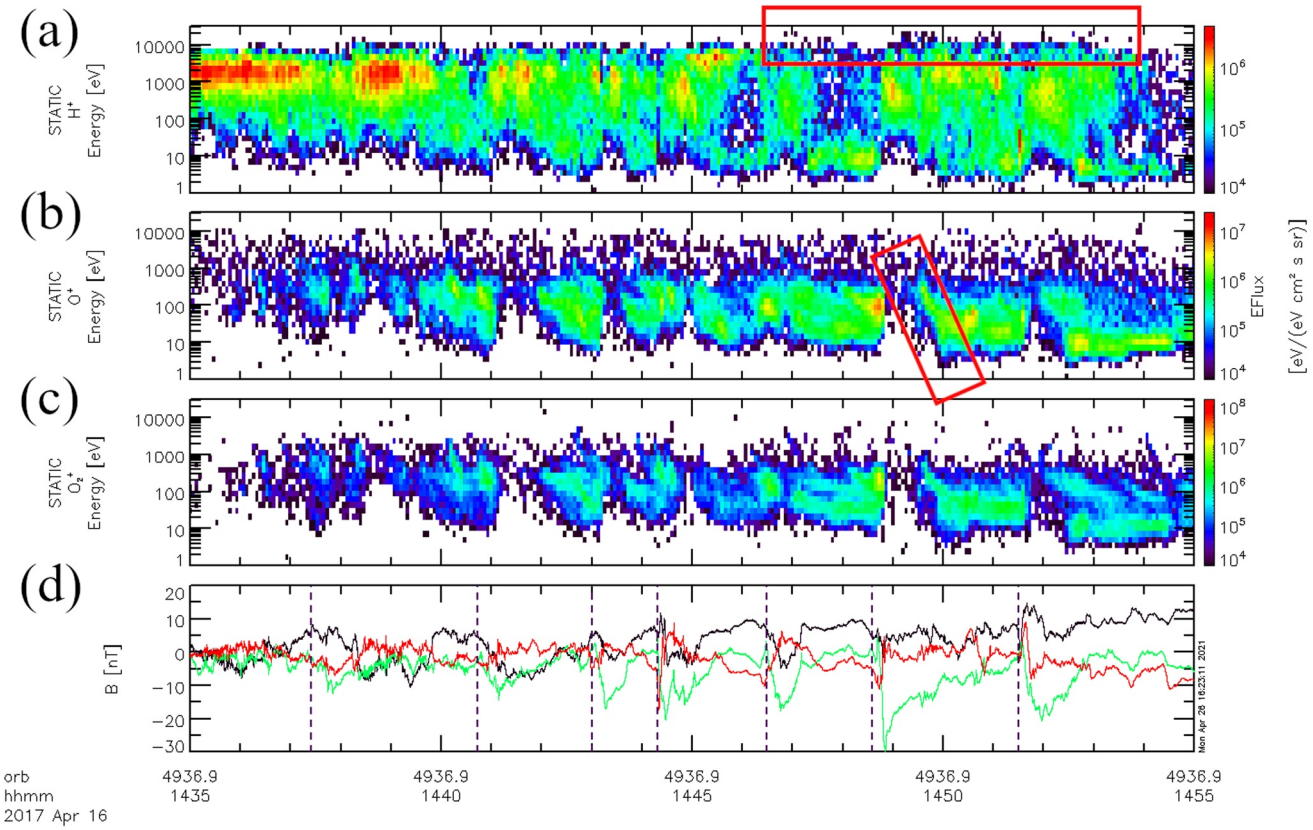

Figure 4. Panels (a–c): Time-series energy spectrograms for H+, O^+, and O_2^+, respectively. The horizontal red box in Panel (a) marks the observation of H^+ with energies much higher than typical solar wind, while the tilted red box in Panel (b) denotes an example of ion energy dispersion corresponding to the encounter of the leading edge of a K–H vortex. Panel (d): *x*, *y*, and *z*-components of the magnetic field measurements; the components are plotted in similar format as Panel (a) of Figure 2 with the vertical dashed lines denoting the magnetic field sawtooth signatures associated with the K–H vortices.

2.3. Mixing Region Within Kelvin–Helmholtz Vortices

The co-existence of magnetosheath and planetary plasma population within the vortex structure is another characteristic feature of K–H vortices formation and the presence of this mixing region allows for mass and energy transport across the flow shear boundary layer via kinetic-scale processes. Figures 4a–4c shows STATIC energy flux spectrograms of the closed-up interval similar to Figure 2 for H^+, O^+, and O_2^+, respectively. Figure 4d shows the three components of the magnetic field measurements for reference purposes. At the start of the interval, the observations of protons with broad range of energies between 100 eV and 10 keV and peak energy at ~1–2 keV and the absence of heavy ions indicates that the spacecraft is in the magnetosheath as mentioned earlier. The STATIC instrument then observed quasi-periodic variations in the energy flux spectrograms of all three ion species that corresponds to the magnetic field perturbations associated with the encounter of each regions of a K–H vortex wave cycle before entering the induced magnetosphere/ionosphere, which is characterized by the presence of only cold planetary protons and heavy ions with energies below 10 eV.

We will use the same wave cycle shown in Figure 3 as an example to illustrate how the variations in the energy spectrograms aligned with that in the magnetic field measurements. MAVEN first observed the presence of mostly cold protons (i.e., energies of ~10 eV) and planetary heavy ions with energies between ~10 and 100 eV between ~14:48:46 and ~14:51:45 UTC. Note that MAVEN also observed a weak presence of 1 keV protons, which suggest that the spacecraft is likely to be located at the lower part of the vortex structure nearer to the induced magnetosphere. The spacecraft then crossed the boundary layer at the trailing edge of the previous vortex into the magnetosheath at 14:48:46 UTC as shown by the simultaneous observation of (a) sawtooth magnetic field signature, (b) "dropout" of heavy ions, and (c) presence of protons with

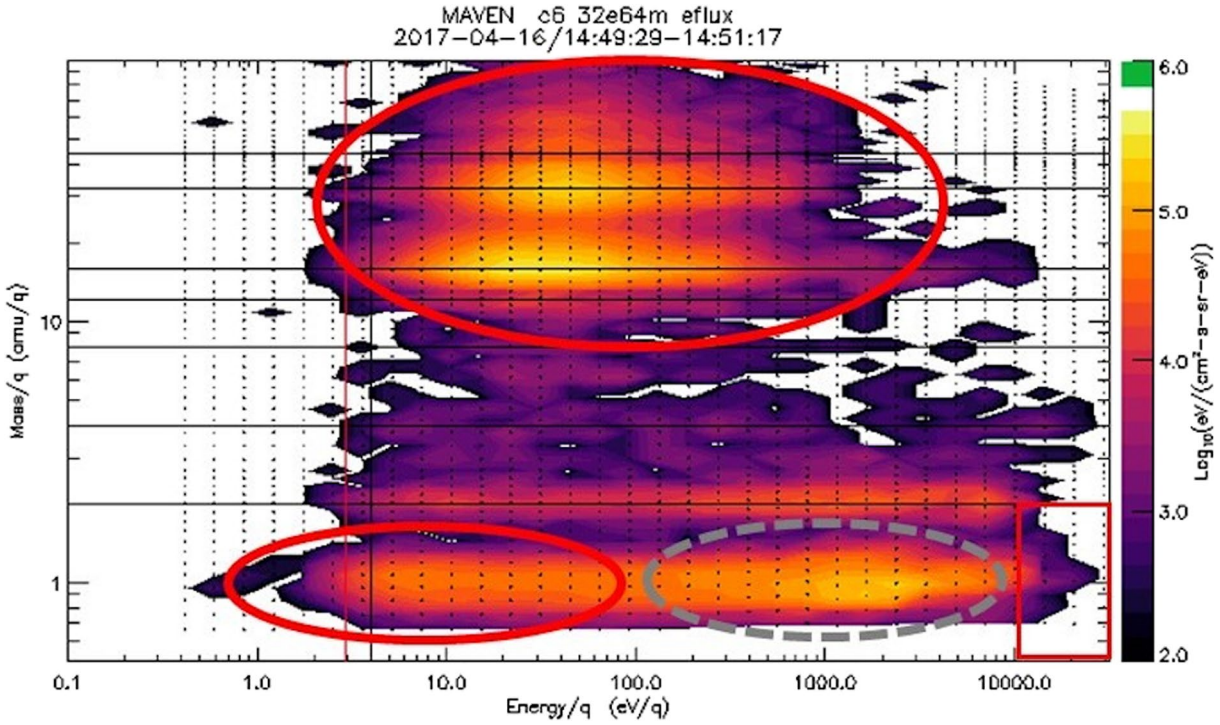

Figure 5. Mass – energy spectrogram measured by the STATIC instrument between 14:49:29 and 14:51:17 UTC. Observations of the co-existence of cold planetary protons (red solid circle at mass/$q \sim 1$) and heavy ions (red solid circle at mass/$q > 10$), and hotter magnetosheath protons (circle with gray dashed lines) strongly suggests the existence of a mixing region within the K–H vortex. The red solid rectangle denotes the part of the spectrogram which shows the presence of protons with energies higher than 10 keV.

magnetosheath-like energies. As the spacecraft subsequently encountered the leading edge of the next K–H vortex at ~14:49:30 UTC, MAVEN did not just observe protons with magnetosheath-like energies, but also cold planetary protons and heavy ions. As shown in Figure 5, simultaneous observations of cold planetary protons and heavy ions (red solid circles), and magnetosheath protons (gray dashed circles) within the K–H vortex is also evident in the mass-energy spectrogram averaged over the time interval when the vortex structure is observed. Protons with energies higher than typical solar wind proton energies shown in the red boxes in Figures 4 and 5, and are discussed in Section 3.1.

We further examined the proton distribution of different regions within a K–H wave cycle to confirm the mixing of magnetosheath and planetary plasma within the vortex structure. Figure 6 shows the energy flux – energy distributions (EFDs) and velocity distribution functions (VDFs) for three different regions of the K–H wave cycle example mentioned above at times (a) 14:48:25 UTC (i.e., trailing edge of the previous K–H vortex before crossing of the boundary layer or spine), (b) 14:48:25 UTC (i.e., magnetosheath region between consecutive K–H vortices), and (c) 14:50:01 UTC (i.e., the mixing region within the K–H vortex). The red dashed lines in Figure 6 shows the EFD and VDF observed in the magnetosheath region at ~14:31:00 UTC, which serve as a reference for typical representation of signatures observed in the magnetosheath. Figure 6a shows a clear "double peak" in the EFD with maximas at ~10 eV and ~1 keV corresponding to the cold (~1–100 eV) planetary protons and hot (>100 eV) magnetosheath protons, respectively. The EFD of the second K–H vortex at 14:50:01 UTC (Figure 6b) also shows similar double-peak distribution in the energy flux, although hotter magnetosheath (colder planetary) protons with peak energy flux at ~3 keV (~4 eV) and a significant population of warm (~20–200 eV) protons were observed as compared to that of the previous vortex shown in Figure 6a. Moreover, the VDFs observed in both K–H vortices show a two-component Maxwellian distribution functions indicative of the presence of two distinct proton population with different temperatures, thereby providing further support for the co-existence and mixing of magnetosheath and planetary protons within the K–H vortices suggested by earlier observations. Note that the EFD and VDF of the magnetosheath "gap" region between the consecutive K–H vortices shown in Figure 6b are consistent

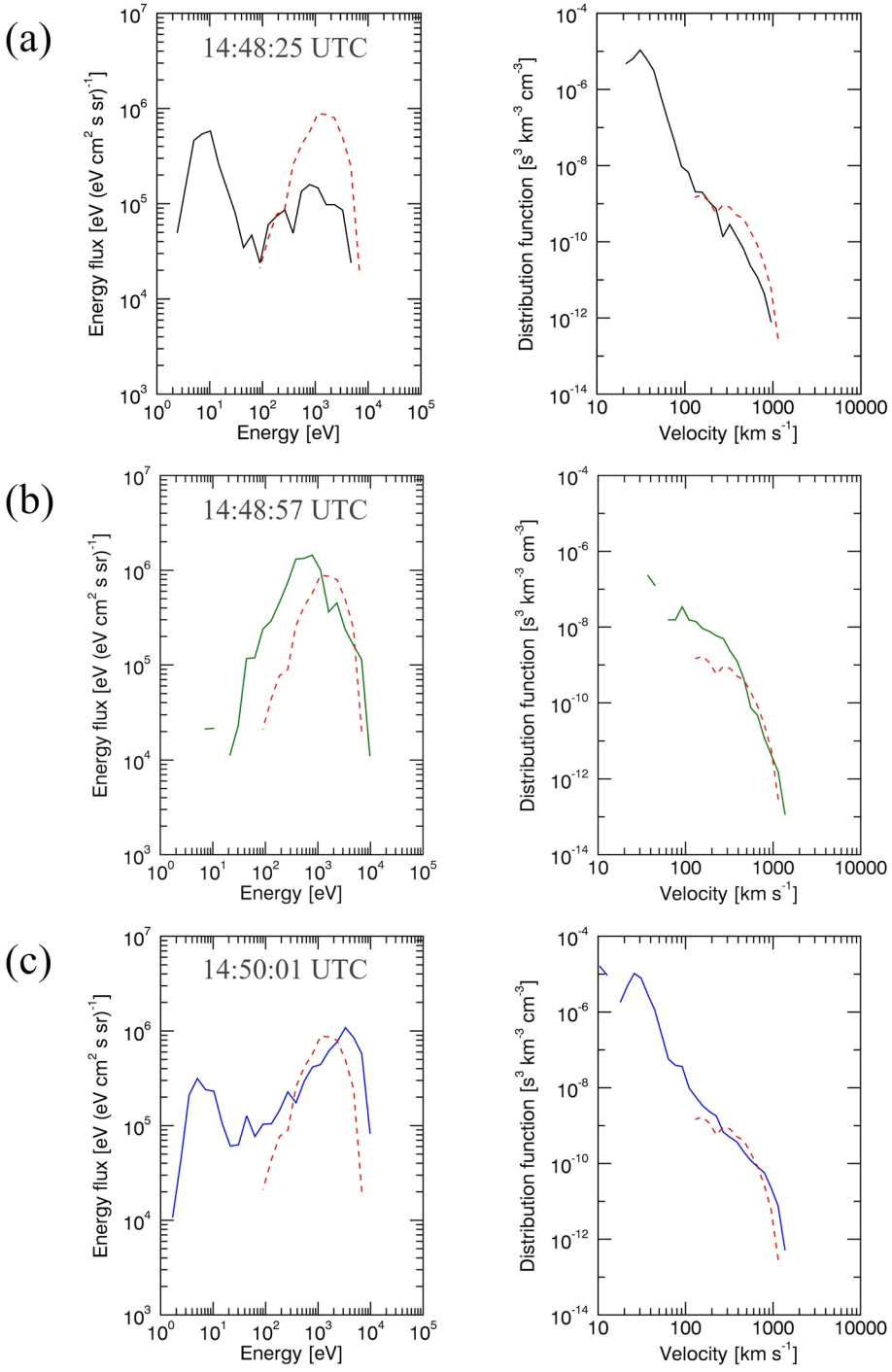

Figure 6. The proton energy flux – energy (left column) and velocity (right column) distribution functions for (a) 14:48:25 UTC, (b) 14:48:57 UTC, and (c) 14:50:01 UTC. The dashed red line represents the typical energy flux – energy and velocity distribution functions observed in the magnetosheath region at 14:31:00 UTC.

with the typical proton distribution in the magnetosheath (red dashed lines), despite the slight disagreement due to the overall gradual decrease in magnetosheath proton energies as the spacecraft travels deeper into the induced magnetosphere.

3. Simulation of Kelvin–Helmholtz Instability at Mars

We carried out a three-dimensional meso-scale MHD simulation of the K–H instability to be compared with the MAVEN data. The full set of the normalized resistive MHD equations is solved by a leap-frog scheme (Birn, 1980; Otto, 1990; Potter, 1973). All physical quantities are normalized to a typical value, that is, scale length $L_0 = 452$ km, magnetic field $B_0 = 11$ nT, number density $n_0 = 5.65$ cm^{-3}, velocity $v_0 = 100.8$ km/s and time $t_0 = L_0/v_0 = 4.48$ s. The simulation domain is a cube with the following dimensions: $|x| \le L_x = 20$, $|y| \le L_y = 30$, and $|z| \le L_z = 40$, which are resolved by 201 grid points along each direction (i.e., uniform along the x-direction with $\Delta x = 0.1$, and non-uniform along the y- and z-directions with the highest resolution of $\Delta y = 0.15$, and $\Delta z = 0.2$ in the center). The x-direction is against the magnetosheath flow direction, and the spatial domain size in the x-direction correspond to a K–H wavelength of ~18,000 km (~5 R_M). The choice of the simulation box length is appropriate since the K–H wavelength was estimated, using the average period observed by MAVEN and inferred phase velocity, to be ~6 R_M (see Section 4.3 for detailed calculations). In the simulation, the ratio between the initial shear flow half-width a and the K–H wavelength in the x-direction is chosen such that $2\pi ka$ is close to ~0.5–1, which corresponds to the highest K–H growth (Miura & Pritchett, 1982). From the simulation set-up, the thickness of the boundary layer (i.e., mixed plasma) is ~901 km, which is a reasonable estimate as the statistical thickness of the boundary layer at Mars ranges from ~0.05 R_M (~169 km) at the subsolar region to ~0.2 R_M (~678 km) near the flanks (Gruesbeck et al., 2016). The y-direction is the normal direction of the shear flow layer, which points from the magnetosphere to the magnetosheath. Hence, the upperhalf domain (i.e., $y > 0$) is referred to as the magnetosheath side, while the bottom half domain (i.e., $y < 0$) is referred as the Martian induced magnetospheric side. The z-direction is determined by the right-hand rule. A frictional boundary condition has been applied along the z-direction to mimic the magnetic field line moving with the magnetosphere and magnetosheath (Ma et al., 2017). Therefore, we can easily define a magnetospheric magnetic field line by tracing the magnetic field line from one of the boundaries at constant z (e.g., $[x_1, y_1, L_z]$) to the other boundary (e.g., $[x_2, y_2, -L_z]$): If both y_1 and $y_2 < 0$, the magnetic field line is a magnetospheric magnetic field line. To calculate the mass loss from the Martian induced magnetosphere through the magnetic reconnection process, we integrated the density along the magnetosphere field line and compared to the initial condition. In order to compare with the particle loss estimated from observations and earlier studies, we converted the mass density calculated from the simulation to the number of the particles by assuming that the ions in the magnetosphere are all O^+.

The initial state of the simulation is a one-dimensional transition layer given by the equation $F = \bar{F} + \delta F \tanh(y)$, and $v_y = v_z = B_y = 0$, where $F = [\rho, v_x, B_x, B_z]$, $\bar{F} = \frac{1}{2}(F_{msp} + F_{msh})$, $\delta F = \frac{1}{2}(F_{msh} - F_{msp})$. The subscripts "msp" and "msh" refer to the induced magnetosphere and magnetosheath values. In this simulation, $F_{msh} = [0.35, -1.94, 0.23, 0.127]$ and $F_{msp} = [2.83, 1.94, 1.356, 0.84]$. The thermal pressure is determined by the total pressure balance, in which the plasma beta in the induced magnetosphere side is 0.5. To trigger the K–H instability, a small single mode perturbation has been applied, which is given by $v_x = [\nabla\Phi \times e_z] f(z)$, where $\Phi(x, y) = \delta v_0 \sin(k_x x)\cosh^{-1}(y/D)$, $f(z) = 1/2\left[\tanh(z + z_0/dz) - \tanh(z - z_0/dz)\right]$, $v_0 = 0.048$, $k_x = \pi/L_x$, $D = 2$, $z_0 = 15$, $dz = 3$. Note that this perturbation is not an exact normal mode, that is, a solution of the linearized equations, but the spectrum of the perturbation has a dominant contribution to the normal mode with the chosen wave number (Ma et al., 2017). We would also like to point out that the simulation coordinate system is different from the observational frame, and a simple Galilean transformation (i.e., $x = x' + vt$) has been applied so that the simulation frame is mostly moving with the K–H vortex. One should also keep in mind that the initial conditions used in the simulation represent our "best-guess estimate" of the instability onset conditions due to the lack of knowledge of the actual initial plasma and fields observations in the magnetosheath and in the induced magnetosphere. Interestingly, our simulation was able to reproduce many of the observational features consistent with those observed by MAVEN as discussed in the earlier sections.

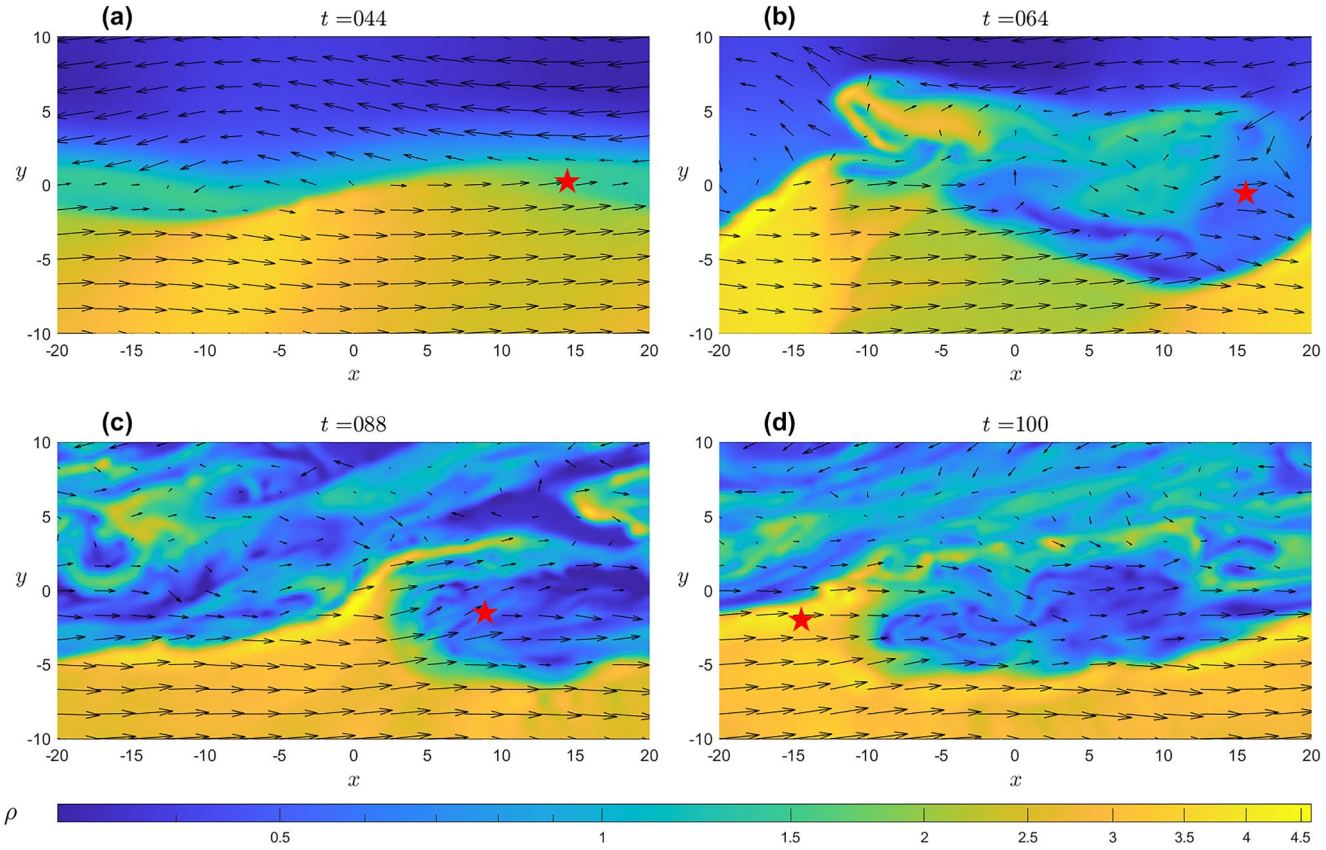

Figure 7. 3-D time-dependent simulation of the plasma density (ρ) in the x-y plane ($z = 0$). Black arrows represents the plasma flow vectors. The $y > 0$ domain is referred to as the magnetosheath side, while the $y < 0$ domain is referred as the martian induced magnetospheric side. Red star represents the virtual spacecraft in the simulation. The virtual spacecraft is traveling at a speed of $v = [1.9445, -0.04]\ v_0$ km/s in the vortex-moving frame (or simulation frame).

3.1. Simulation Results

Figure 7 show the time evolution of our simulated K–H instability in the xy-plane at four simulation time steps $t = 44$, 64, 88, and 100, with $y = 10$, $y = -10$, and $|y| < 1$ corresponding to the regions consisting of magnetosheath plasma, inner magnetospheric/planetary plasma, and mixed plasma, respectively. Figure 7a (i.e., $t = 44$) shows that the K–H wave is excited along the flow shear boundary during the initial development of the K–H instability. A partially developed K–H vortex is quickly formed at $t = 64$ (Figure 7b) as shown by the initial steepening of the shear boundary at the trailing edge of the partial vortex. Interestingly, our simulation also indicated that secondary instabilities were beginning to form along the edges of the vortex at $t = 64$, which could possibly explain the lack of clear bipolar signatures in the velocity component perpendicular to the unperturbed boundary. The K–H vortex is fully rolled-up by $t = 88$ (Figure 7c) during the non-linear stage of the K–H instability, allowing for the mixing of magnetosheath and planetary plasma in the mixing region at the leading edge of the vortex. During the later stage of the vortex evolution at $t = 100$ (Figure 7d), these secondary instabilities distorts the structure of the vortex, and can facilitate efficient transport of the mixed magnetosheath and planetary plasma, which are originally confined within the vortex, across the shear boundary layer. The simulation animation is provided in Supporting Information S1.

Figure 8a shows the time series measurements of (i) magnetic field, (ii) proton density, (iii) proton velocity, and (iv) magnetic and total pressure measured by a virtual spacecraft from the 3-D MHD simulation. Note that the simulation results in Figure 8a are displayed in the same coordinate system as the MAVEN observations for comparison. Figure 8b shows an example of a K–H vortex observed by the MAVEN spacecraft with format similar to Figure 8a. It is evident that the 3-D MHD simulations results agree very well with our MAVEN observations of fully developed K–H vortices at Mars. In particular at $t \sim 4$ min, the MHD

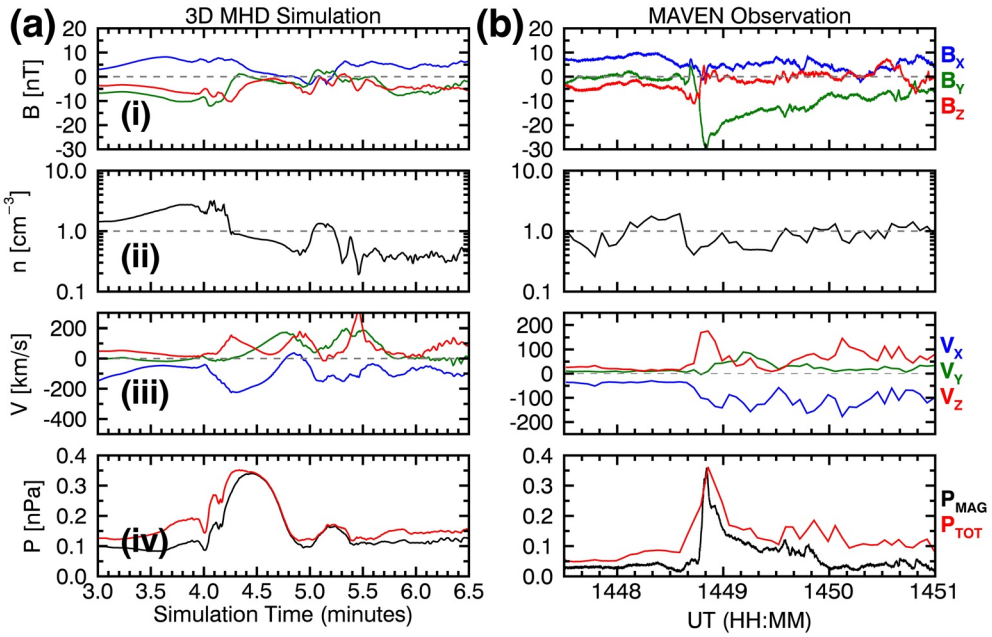

Figure 8. (a) Time series (i) magnetic field in *x*, *y*, and *z*-components, (ii) proton density, (iii) plasma flow velocity, and (iv) magnetic and total pressure measurements observed by the virtual spacecraft in the 3-D MHD simulation. (b) Time series of MAVEN observation of a K–H vortex example with format similar to Panel (a). Both simulation and observation results are display in similar coordinate system for comparison. The close agreement between the magnetic field and plasma measurements predicted by the 3-D MHD simulation, and MAVEN's observation supports the scenario for the occurrence of K–H instability along the Martian induced magnetosphere boundary.

simulation results also shows (a) sawtooth-like perturbations in all components of the measured magnetic field vectors with anti-correlated B_Z maxima and B_X minima, followed by a return to background magnetic field values and (b) a decrease in proton density that coincides with the sawtooth magnetic field signature. Note that B_Y (out-of-plane direction) also shows magnetic field signatures similar to B_Z, indicating a twisted magnetic field topology within the vortex structure. An expected tailward (negative *x*-direction) and northward (positive *z*-direction) enhancement in the plasma flow is also observed in the simulation results at the same time as the magnetic field perturbations, which is consistent with the plasma measurements observed in our MAVEN observation results. Not surprisingly, the total pressure enhancement observed in the simulation results, which is similar to that observed in our MAVEN observations, strongly indicates that the simulated structure is indeed a K–H vortex, instead of a magnetic flux rope. The excellent agreement between our observational and simulation results, in terms of the expected magnetic field and plasma signatures of a fully developed vortex structure due to K–H instability at Mars, provides clear evidences that MAVEN indeed observed a vortex structure associated with the non-linear development of K–H instability along the Martian induced magnetospheric boundary.

3.2. 3-D MHD Simulation of Plasma Transport Due to 3-D Reconnection in K–H Vortices

In three-dimension, K–H instability can also generate reconnection below and above of the shear flow plane, which can allow for more efficient plasma transport (Ma et al., 2017). The top panel of Figure 9 shows the number of particles in the flux rope created by 3-D reconnection in the vortices as a function of time determined from the simulation results presented in Section 3.1. We calculated the gradient of the linear fit to the data points (red line), which represents particle loss rate, to be $\sim 9 \times 10^{23}$ particles/s. The bottom panel shows the magnitude of the velocity component normal to the initial boundary as a function of time on a log-scale (blue line). We calculated the gradient of the exponential fitting, which represents the K–H growth rate, to be ~ 0.0184 s^{-1}. Note that the MHD description can only address particle loss through the double reconnection process driven by the non-linear K–H wave. The particle mixing due to finite gyroradius requires additional test-particle or hybrid simulations (Ma et al., 2019). Thus, the major particle loss

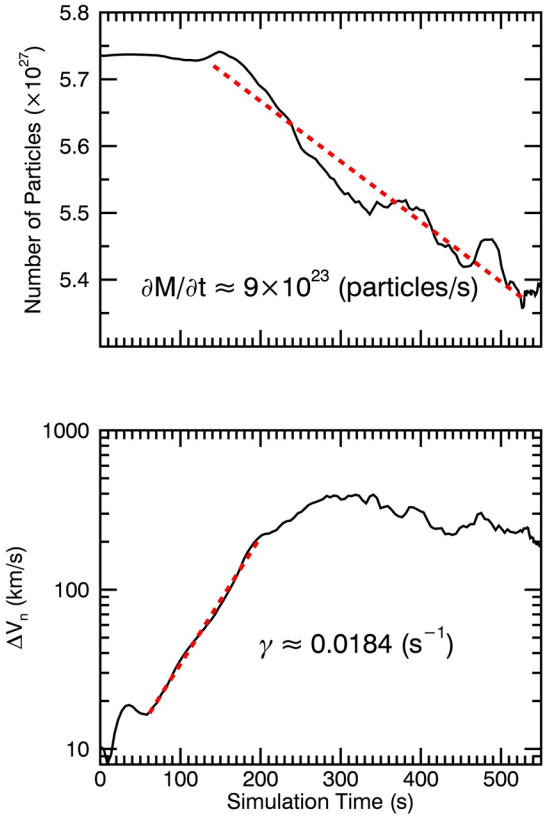

Figure 9. (Top) Number of particles in the closed magnetospheric flux tube in the 3-D MHD simulation as a function of time. Red line represents the linear fit and its gradient represents the particle loss rate. (Bottom) Magnitude of velocity component normal to the initial boundary as a function of time on a log-scale. The gradient of the exponential fitting represents the K–H growth rate γ.

happens after the K–H instability reaches the non-linear stage. We would like to note that the K–H instability growth rate and particle loss rate due to K–H instability calculated from our simulation results are similar to the growth rate ($\sim 10^{-2}$ s^{-1}) and loss rate ($\sim 10^{23}$ particles/s) calculated from the earlier theoretical study by Penz et al. (2004).

4. Discussion

In this study, we presented magnetic fields and plasma signatures of fully developed K–H vortices observed by MAVEN on April 16, 2017 during an encounter of Mars' induced magnetosphere boundary near the polar terminator in the Northern Hemisphere. The observations presented above lead us to the unambiguous conclusion that MAVEN had indeed observed a wave train of fully developed vortices associated with the development of K–H instability in its non-linear stage along the induced magnetosphere boundary passing over the MAVEN spacecraft. These include (a) the quasi-periodic, sawtooth-like magnetic field perturbations, (b) corresponding variation pattern in the proton and heavy ions plasma measurements (i.e., density and velocity), and (c) simultaneous presence of magnetosheath protons with planetary ions in regions identified as the mixing regions of the vortices. Furthermore, the absence of a maxima in the magnetic field intensity and total pressure at the center of the bipolar-like sawtooth magnetic field signature, and minimum variance analysis results strongly indicate that the observed structures are K–H waves rather than magnetic flux ropes. These MAVEN observations were further supported through MHD simulations of K–H instability at Mars using inputs from MAVEN measurements as initial conditions. The model results demonstrated strong corroboration with MAVEN's observed signatures of fully developed vortices associated with the occurrence of K–H instability along Mars' induced magnetosphere boundary.

4.1. Magnetic Reconnection in KH-Induced Vortices

At the non-linear stage of the instability, the K–H vortices can twist the magnetic field in the flow shear plane (i.e., *xz*-plane in the case study presented here) and create regions of thin current sheets with reconnecting anti-parallel field lines. Hence, the natural follow-up question to our observations of K–H vortices at Mars would be: did MAVEN observe any signatures of magnetic reconnection in the vortices? We would like to point out that MAVEN observed the minor presence of protons with energies higher than the solar wind's (i.e., $E > 10$ keV) highlighted by the red box in Figure 4a. Similar 10 keV proton population was also observed in the mass-energy spectrogram displayed in Figure 5 and this high-energy proton signature is most notable near the leading edge of the K–H vortex observed at ~14:50 UTC. Note that during the time interval highlighted by the red box in Figure 4a, STATIC observed an average count rate of ~2–4 protons per 4 s measurements. There are typically zero counts at energies greater than 10 keV observed by STATIC in the Martian magnetosheath, which indicates that these energized protons with energies greater than 10 keV observed by STATIC are physical and not a result of instrumental background. Furthermore, MAVEN observed signatures of ion (proton and heavy ions) energy dispersion, where the spacecraft observed faster, more energetic ions followed by the slower, less energetic ions near the leading edge of the vortices. An example of the O^+ energy dispersion is shown by the tilted red box in Figure 4b. Both observations seems to suggest energization and acceleration of ions mostly at the edges of the vortex. A possible acceleration mechanism is magnetic reconnection, which converts magnetic field energy into particle kinetic energy and accelerates ions (and electrons) to Alfvénic speed in the outflow exhaust region.

The single-spacecraft analysis technique commonly used to test for signatures of reconnection (or rotational discontinuity) is the Walén test, which compares plasma velocities in a quasi-stationary frame of reference with the local Alfvén velocity using the Walén relation (Sonnerup et al., 1995). The relation states that in ideal MHD, the accelerated plasma flow for a rotational discontinuity is Alfvénic in the deHoffmann–Teller (HT) frame, where the electric field ideally "vanishes" (deHoffmann & Teller, 1957). The reader is referred to Khrabrov and Sonnerup (1998) for details on the determination of the HT frame velocity. The Walén relation can be expressed by the following equation:

$$\mathbf{V}' = \mathbf{v} - \mathbf{V}_{HT} = \pm\mathbf{V}_A = \pm\mathbf{B}\frac{\sqrt{1-\alpha}}{\sqrt{\mu_0\rho}} \tag{2}$$

where $\mathbf{V}'$ is the plasma velocity in the HT frame of reference, $\mathbf{V}_{HT}$ is the HT frame velocity, $\mathbf{v}_A$ is the Alfvén velocity corrected for pressure anisotropy and α is the pressure anisotropy factor given by the expression:

$$\alpha = \frac{P_{\parallel} - P_{\perp}}{\mu_0 B^2} \tag{3}$$

If MAVEN did indeed encounter a magnetic reconnection region within the K–H vortices, it would have observed a good (a) HT frame (i.e., strong correlation between each components of the convective electric field $\mathbf{E}_c = -\mathbf{v} \times \mathbf{B}$ and HT electric field $\mathbf{E}_{HT} = -\mathbf{V}_{HT} \times \mathbf{B}$) and (b) agreement with the Walén relation (i.e., strong correlation between each components of the plasma velocity in the HT frame and Alfvén velocity). Ideally, the correlation coefficients should be near unity for a good HT frame determination and a successful Walén test. The gradient of the linear regression line fitted to the $\mathbf{V}'$–$\mathbf{v}_A$ scatterplot should also be ∼1 (i.e., Alfvénic plasma flow) if the Walén relation is satisfied (Sonnerup et al., 1995). A similar analysis method had also been used to search for signatures of magnetic reconnection in K–H vortices by Nykyri et al. (2006) using Cluster observations.

We computed the time-series HT frame velocity for each plasma data point over the entire 20-min interval shown in Figure 2 using a sliding time window of 90 s and performed the Walén test for each 90-s-long sub-interval. The results for the HT analysis and Walén test are displayed in Figure 10. As shown in Panels (ii–iv) of Figure 10a, the HT frame between 14:37 and 14:53 UTC is well-determined with an average correlation coefficient (R) between convective and HT electric field (black line) of ∼0.93 and mean $\mathbf{V}_{HT} \sim [-150, 51, 76]$ km/s. The highly fluctuating low correlation coefficient between the plasma velocity in the HT frame and Alfvén velocity (red line), on the other hand, indicates that the Walén test generally did not perform well, except for the interval centered at ∼14:40 UTC corresponding to the vortex region (labeled as Vortex 1) of the K–H wave where a peak correlation coefficient of ∼0.85 was observed. The $\mathbf{E}_c$–$\mathbf{E}_{HT}$ and $\mathbf{V}'$–$\mathbf{v}_A$ scatterplots for this sub-interval is shown in the top left and top right panels of Figure 10b, respectively. A high correlation coefficient of ∼0.95 shown in the $\mathbf{E}_c$–$\mathbf{E}_{HT}$ scatterplot indicates the existence of a well-determined HT frame, while the $\mathbf{V}'$–$\mathbf{v}_A$ scatterplot also shows a reasonably good correlation coefficient of ∼0.85. Note the presence of anti-sunward (negative) flow in the HT frame in the $\mathbf{V}'$–$\mathbf{v}_A$ scatterplot consistent with the vortex motion of the plasma within the mixing region. Interestingly, the Walén test further shows a regression line slope of ∼0.52, which is smaller than unity as predicted by the Walén relation. Our analysis suggests that the plasma flow is sub-Alfvénic in the HT frame (Øieroset et al., 2000) and similar Walén test results are typically observed for slow-mode shocks in outflow regions of fast reconnection (Petschek, 1964). The simultaneous existence of a high-quality HT frame of reference and successful Walén analysis provides strong evidences for magnetic reconnection within the vortex region of a K–H wave.

The bottom panels of Figure 10b show the HT analysis and Walén test results for a later time interval between 14:49:31 and to 14:50:59 UTC (labeled as Vortex 2), where we had identified earlier as the mixing region of the K–H wave cycle. Note that since Vortex 2 is observed later in time, it is located further upstream than Vortex 1 as shown by MAVEN's trajectory in Figure 1a. The $\mathbf{E}_c$–$\mathbf{E}_{HT}$ scatterplot shows a lower correlation coefficient of ∼0.81, which indicates a less accurate, but still within reasonable level of confidence, determination of the HT frame. However, a poor correlation coefficient between $\mathbf{V}'$ and $\mathbf{v}_A$, and regression slope << 1 indicates that the Walén test had failed and the observed magnetic field and plasma signatures could not be interpreted as the encounter of a rotational discontinuity or a slow-mode shock in the KH–induced vortex region observed at a later time. Our analysis results then begs the question of why Vortex 1,

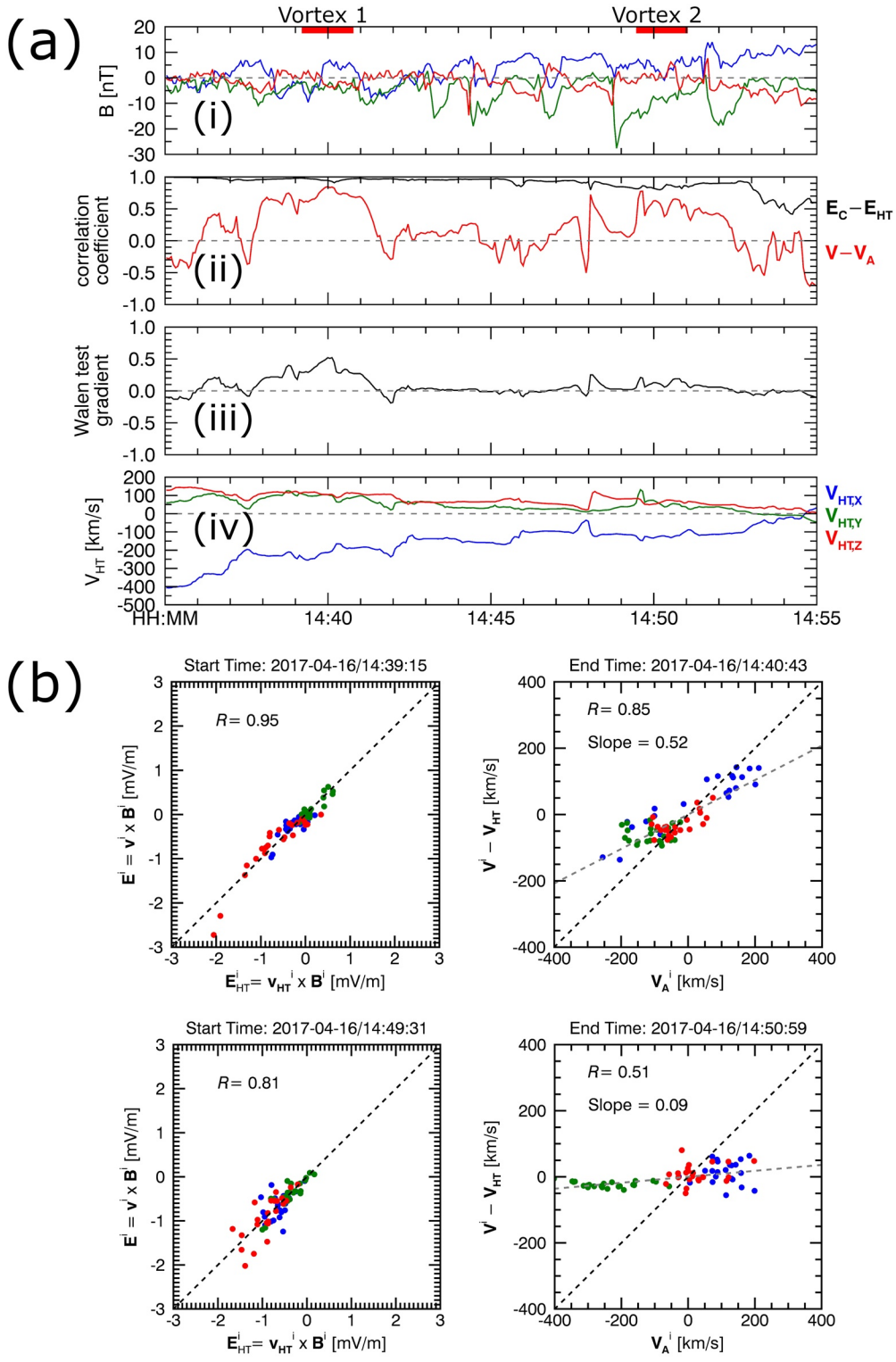

Figure 10. (a) Panel (i): *x*, *y*, and *z*-components of the magnetic field measurements. The components are plotted in similar format as Panel (iv) of Figure 4. Panels (ii and iii): Time-series correlation coefficients of the $\mathbf{E}_C$–$\mathbf{E}_{HT}$ (black) and $\mathbf{V}'$–$\mathbf{v}_A$ (red) scatterplots, and gradient of the regression line fitted to the $\mathbf{V}'$–$\mathbf{v}_A$ scatterplot, respectively, using a sliding time window of 90 s. Panel (iv): Time-series HT velocity computed from the deHoffman-Teller analysis technique. (b) (Top row panels): $\mathbf{E}_C$–$\mathbf{E}_{HT}$ and $\mathbf{V}'$–$\mathbf{v}_A$ scatterplots for time interval 14:39:15–14:40:43 UTC (red bar) corresponding to MAVEN observation of Vortex 1. Each data point plotted represents the *x* (blue), *y* (green), and *z* (red) – components of each vector parameter plotted in the scatterplot. (bottom row panels): $\mathbf{E}_C$–$\mathbf{E}_{HT}$ and $\mathbf{V}'$–$\mathbf{v}_A$ scatterplots for time interval 14:49:31–14:50:59 UTC (red bar) corresponding to MAVEN observation of Vortex 2 in similar format as the top panels. The Walén analyses provides evidence for the possibility of magnetic reconnection occurring within the mixing region.

which was observed first by MAVEN at ~14:40 UTC, shows the possibility of reconnection occurring within the vortex structure, while Vortex 2 at ~14:50 UTC, which was observed later, does not? One plausible explanation is the observation of time evolution of K–H vortices in the non-linear stage of the K–H instability. The fact that Vortex 1 was observed further downstream than Vortex 2 suggests that Vortex 1 has already begun the decaying stage of the instability via vortex-induced reconnection, while Vortex 2 is still at its early non-linear development stage of the K–H instability. Note that this explanation is also consistent with the magnetic field measurements, where the sawtooth signatures commonly associated with the development of K–H vortices is not as clear in Vortex 1 as compared to that of Vortex 2. Furthermore, recent simulations by Nakamura et al. (2020) suggested that clear K–H signatures may be observed only for a short period of time as the occurrence of fast reconnection induced at different locations of the vortex during early non-linear stage leads to the quick decay of vortex structure.

A possible source of error for our Walén analyses is the small temporal and spatial scale in which magnetic reconnection is occurring within the K–H vortex region. Since the STATIC instrument takes 4s to measure a full plasma distribution, any transient variations (i.e., magnetic reconnection) that occur on time scales shorter than 4s would be "smeared out." We would like to further point out that although STATIC does not cover the full sky (field-of-view of the instrument is 360 × 90° [McFadden et al., 2015]), detailed analysis of the STATIC's energy-mass-direction data (not shown here) indicates that STATIC captured the majority of the distribution functions during the time interval shown in Figure 4. In addition, the Walén analysis presented in this study only considered protons and not the heavy ions, which may aggravate the impact of inaccurate $\mathbf{v}_A$ on the correlation coefficient and regression slope. Further study is required to investigate the effects of heavy ions on the Walén analysis results. We would also like to point out an alternate explanation for the poor Walén relation at the flow shear plane due to the possibility of three-dimensional reconnection occurring within the K–H vortices as shown in the 3-D simulations presented in Section 3. Nonetheless, the overall conclusion that magnetic reconnection occurred during at least some of the observed vortices remains robust given the Walén test for Vortex 1.

4.2. Kelvin–Helmholtz Instability Growth Rate

In the previous section, we have presented unambiguous observations of K–H instability induced vortices formed along the KH-unstable induced magnetosphere boundary, which naturally motivates us to estimate the growth rate of K–H instability for this case event. Earlier theoretical (Penz et al., 2004) and observational (Ruhunusiri et al., 2016) studies incorporated viscous and finite Larmor radius (FLR) effects in their calculations of the linear growth rate of K–H instability. Following the methodology outlined in Wolff et al. (1980), we examine the condition in which the effects of viscous and FLR are important by considering the dimensionless gyroviscosity Reynolds number Re_g given by the equation:

$$Re_g = \frac{UL}{\nu_L} = \frac{UL}{\frac{1}{4}R_L^2\Omega_L} \tag{4}$$

where U is the typical velocity of the system, L is the characteristic K–H wavelength, and ν_L is the effective gyroviscosity coefficient. FLR effects are negligible when Re_g is >> 1 and gyroviscous effects cannot be ignored when Re_g is close to unity (Wolff et al., 1980). We first estimated the Larmor radius R_L and proton gyrofrequency Ω_L to be ~110 km and 1 s^{-1}, using B ~10 nT and $\nu_\perp$ ~110 km/s, respectively. We also calculated the characteristic K–H wavelength L to be ~2.1 × 10^4 km (or ~6 R_M), assuming that the K–H waves are instantaneously traveling at the mean HT velocity of ~175 km/s with an average time period of ~2 min. We then calculated the gyroviscosity Reynolds number using Equation 4 to be ~10^3. Since the gyroviscosity Reynolds number is much larger than 1, we argue that the FLR effects are negligible and can be ignored in our calculations of the growth rate. Since the gyro-radius of planetary O^+ and O_2^+ at ~50 eV (~408 and ~577 km, respectively) << characteristic length L, FLR effects by the heavy ions can also be ignored. Note that the effects of FLR can be significant in the case of a velocity shear layer with finite thickness. The larger the ratio between the ion gyroradius and the half-width of the velocity shear layer, the larger the effects of FLR (Henri et al., 2013; Nakamura et al., 2010).

The linear growth rate for K–H instability in the collisionless MHD plasma regime is then given by the equation (Chandrasekhar, 1961):

$$\gamma^2 = \frac{\rho_1\rho_2}{\left(\rho_1+\rho_2\right)^2}\left[\boldsymbol{k}\cdot\left(\mathbf{v}_1-\mathbf{v}_2\right)\right]^2 - \frac{1}{\mu_0\left(\rho_1+\rho_2\right)}\left[\left(\boldsymbol{k}\cdot\mathbf{B}_1\right)^2+\left(\boldsymbol{k}\cdot\mathbf{B}_2\right)^2\right] \quad (5)$$

where ρ is the effective mass density including proton and heavy ions, $\mathbf{B}$ is the magnetic field, $\mathbf{v}$ is the plasma flow velocity and $\boldsymbol{k}$ is the wave propagation vector with magnitude inversely proportional to the K–H wavelength (i.e., $k = 2\pi/\lambda \sim 3\times10^{-4}$ km^{-1}). Similar to Equation 1, the subscript indices (1 and 2) represents parameters corresponding to the magnetosheath and the induced magnetosphere. To simplify the calculations, we assumed the wave propagation vector (or k-vector) to be in the x-direction (i.e., $\boldsymbol{k} = k\,\hat{\mathbf{x}}$). Using the plasma density measured by the STATIC instrument shown in Figure 2, we first calculated the effective mean mass density (including H^+, O^+, and O_2^+) in the magnetosheath ρ_1 and induced magnetosphere ρ_2 to be ~5.6 m_p and 480 m_p kg cm^{-3}, respectively, where m_p is the mass of a proton. We then determined the mean magnetic field in the magnetosheath (B_1) and induced magnetosphere (B_2) to be ~5 nT and ~15 nT, by averaging over 3-min intervals between 14:30–14:33 UTC and 14:56–14:59 UTC, respectively. Using Equation 4 and a flow shear difference (i.e., $\mathbf{v}_1$–$\mathbf{v}_2$) of ~250 km/s, we estimated the linear growth rate to be ~5.84×10^{-3} s^{-1}.

Our over-simplified, back-of-the-envelope calculation of the linear growth rate for K–H instability at Mars is approximately half of the growth rate ($\gamma \sim 10^{-2}$ s^{-1}) estimated by Penz et al. (2004) for medium solar wind speed (~400 km/s) near the polar terminator and the growth rate calculated from our 3-D MHD simulation results presented in this study ($\gamma \sim 0.0184$ s^{-1}). This discrepancy may be attributed to the assumption that the K–H wave propagates only in the x-direction. Simulations and observations (e.g., Adamson et al., 2016; Nykyri et al., 2006) of K–H vortices at Earth had shown that the k-vector for the K–H waves can have an out-of-plane component to maximize the onset and growth rate of the instability. Furthermore, it is inaccurate to calculate the growth of K–H waves or vortices based on satellite measurements collected during the non-linear stage of the instability while using the equation from linear theory. Since the effect of the instability is to reduce the amount of free energy (velocity shear in this case), calculating the growth rate using measurements at non-linear stage would underestimate it. In reality, single spacecraft measurements are insufficient to resolve the complex structure of the magnetosheath – induced magnetosphere boundary layer. We would also like to emphasize the limitation of using Equation 5 as an approximation for the K–H stability criterion and growth rate which lacks the relevant effect of finite width of the flow shear layer. The equations used for the calculations of the growth rate in this study assumed a sharp boundary across which a plasma flow shear exist, which limits its usefulness when applied to a more realistic structure of the boundary layer. Earlier theoretical studies (e.g., Miura, 1982; Ong & Roderick, 1972; Walker, 1981) on the effects of finite shear boundary layer also indicates a dependency of the growth rate on the half-width of the velocity shear layer. However, since there is no explicit solution to growth rate problem with finite boundary layer width for magnetized plasma, it is out of the scope of this study to further investigate the effect of finite width of the flow shear layer on our estimated growth rate and will be left for future investigation. Therefore, based on the above reasons, we emphasized that our estimated growth rate should only be considered as an approximation, and not be taken as the absolute value. Future theoretical or numerical studies should be carried to further investigate the dependence of the growth rate of K–H instability at Mars on different initial magnetic field and plasma conditions across the magnetosheath – induced magnetosphere boundary layer of finite thickness.

4.3. O^+/O_2^+ Escape Rates Associated With Kelvin–Helmholtz Instability

One of the main consequences of magnetic reconnection occurring in K–H vortices is the formation of detached plasma clouds in Mars (Penz et al., 2004) and Venus (e.g., Brace et al., 1982; Pope et al., 2009), which result in the loss of heavy ions from the Martian ionosphere. Brace et al. (1982) estimated the escape rate of O^+ associated with the detachment of plasma clouds at Venus to be on the order of ~10^7 ions/s while subsequent theoretical study conducted by Penz et al. (2004) estimated the loss of O^+ from K–H instability induced plasma clouds at Mars to be on the order of 10^{23} particles/s for K–H waves occurring near the polar terminator at high altitude (~800 km) under medium-speed solar wind condition (v_{sw} ~400 km/s). The

natural follow-up question will be: what is the instantaneous escape flux of ionospheric heavy ions due to the detachment of plasma clouds results from the K–H vortices observed in the case study presented here? Following the methodology outlined in Brace et al. (1982), we first estimated the volume of a quasi-cylindrical plasma cloud to be $\sim 1.18 \times 10^{21}$ m^3, assuming the K–H instability induced plasma cloud with width of ~ 1 R_M is traveling tailward at a mean HT speed of ~175 km/s and that it takes ~2 min for the vortex to pass the spacecraft. To calculate the total instantaneous escape flux, we first estimate a total of six vortices forming along the surface of the induced magnetosphere boundary at any given time. Note that this is a conservative estimation, as compared to that estimated by Brace et al. (1982), and would serve as a lower limit for the range of possible number of K–H vortices forming along the boundary at any point in time. By further assuming a uniform mean ion density of ~10 particles/cm^3 (Panel [c] of Figure 2) throughout the cylindrical vortex structure, we then estimate the instantaneous escape flux for each heavy ion species to be $\sim 5.90 \times 10^{26}$ particles/s based on our observations. Note that O^+ and $O_2{}^+$ have similar escape rate in our calculations since the STATIC instrument observed equal plasma density as shown in Panel (c) of Figure 2.

Our over-simplified estimation of the heavy ion instantaneous escape rate is consistent with that calculated by Brace et al. (1982) for the Venusian plasma clouds, but at least two orders of magnitude larger than the escape rate calculated by Penz et al. (2004) and the loss rate calculated from our 3-D MHD simulation results in this study ($\sim 9 \times 10^{23}$ particles/s) for mass loss associated with K–H instability at Mars. We will like to point out that the slight order-of-magnitude discrepancy in the instantaneous loss rates could be attributed to our over-estimation of the plasma cloud volume since the mechanisms responsible for ion loss within the K–H vortices (i.e., magnetic reconnection and particle mixing) occur near the flow shear boundary. Hence, the assumption of the entire vortex region as the detached plasma cloud in our calculations could lead to over-estimation of the volume and that our calculation represents an upper limit to the range of possible instantaneous escape rates. Our estimated instantaneous escape rate of $O^+/O_2{}^+$ associated with K–H instability is also approximately two to three orders of magnitude larger than the estimated total average escape rate ranging from $\sim 10^{23}$ to 10^{25} s^{-1} (e.g., Brain et al., 2015; Dubinin et al., 2011), which strongly indicate the potentially significant contribution of the K–H instability induced plasma cloud to the ionospheric mass loss at Mars. However, we have to emphasize that mass loss associated the K–H instability is only relevant when conditions are favorable to the non-linear growth of the K–H instability. As such, it is not a continuous loss process and, depending on the frequency of favorable growth conditions, it is likely to be a minor contributor to the overall ionospheric escape problem at Mars when integrated over the time evolution of the Martian atmosphere.

Our calculation of the instantaneous escape rate associated with K–H instability at Mars further lead us to the question of the solar wind and IMF conditions that favors the onset and non-linear development of K–H instability along the Martian induced magnetosphere boundary. Statistical surveys at Earth demonstrated that the occurrence of K–H instability is influenced by the IMF orientation. Studies have revealed that K–H vortices are predominantly observed during northward IMF condition (e.g., Hasegawa et al., 2006; Lin et al., 2014; Taylor et al., 2012), although they can also be observed during southward IMF direction (Hwang et al., 2011; Yan et al., 2014). Furthermore, the sense of the dawn-dusk asymmetric growth of K–H instability is also dependent on the horizontal component of the IMF, such that a Parker Spiral (Ortho-Parker Spiral) orientation favors K–H instability growth on the dawn (dusk) flank of the terrestrial magnetopause (Henry et al., 2017; Nykyri, 2013).

The problem on the dependency of the non-linear growth of K–H instability on solar wind and IMF conditions, on the other hand, remains largely unexplored and is complicated due to the absence (presence) of a global (crustal) magnetic field. Unfortunately, the trajectory of the MAVEN spacecraft for the orbit studied here remains mostly near or within the induced magnetic field draped around the planet and hence did not observe the solar wind outside of the bow shock. However, our observation of K–H vortices along the polar terminator in the Northern Hemisphere and the lack of clear observations of K–H vortices in prior or subsequent encounter of the induced magnetosphere boundary in the Southern Hemisphere seems to suggest that the presence of the crustal magnetic field might inhibit the growth of K–H instability. It is plausible the complex interaction between the IMF lines and the crustal magnetic field line might stabilize the boundary surface to K–H instability. Further investigation on the topology of the magnetic field lines, similar to recent K–H studies at Earth (e.g., Sisti et al., 2019), should also be conducted to provide better

constraint on the detached plasma cloud volume, and hence plasma loss rates. With the limitations of single-spacecraft measurements, any further discussions on the relationship between K–H instability growth, and solar wind condition and interaction with the crustal magnetic field is out of the scope of this study and as such remains an unanswered question. Therefore, future theoretical and statistical studies must be carried out in conjunction with global simulation studies to investigate the effects of solar wind conditions and presence of crustal magnetic field on the growth of K–H instability along the flow shear boundary. As discussed above, answering these questions will lead to an understanding of the relevancy of the relatively large instantaneous loss rates due to individual periods of K–H instability versus the loss rates integrated over longer time periods.

5. Conclusions and Future Work

The results presented here can be summarized to the following important observations:

1. MAVEN observed fields and plasma signatures, primarily the (a) the quasi-periodic, sawtooth-like magnetic field perturbations, and (b) corresponding density decrease and (c) tailward enhancement of plasma velocity for both protons and heavy ions, associated with the encounter of a wave train of fully developed vortices during the development of K–H instability in its non-linear stage along the Martian induced magnetosphere boundary.
2. The co-existence of magnetosheath and planetary plasma in the region prior to the sawtooth magnetic field signature supports the observation of a mixing region in the K–H vortex, which strongly suggest the transport of mass across the flow shear boundary.
3. Pressure enhancement (minimum) at the edge (center) of the "bipolar-like" sawtooth magnetic field signature and MVA results are consistent with the scenario of K–H vortices formation.
4. The close agreement between the 3-D MHD simulation results, and MAVEN's fields and particles measurements also supports the scenario for the occurrence of K–H instability along the Martian induced magnetosphere boundary.
5. The observation of protons with energies greater than 10 keV and our Walén analyses provides evidence for the possibility of particle energization within the mixing region via either magnetic reconnection, secondary instabilities or other turbulent processes.
6. From the observations, we estimated the lower limit on the instantaneous linear K–H instability growth rate to be $\sim 5.84 \times 10^{-3}$ s^{-1}. We also calculated a growth rate of 0.0184 s^{-1} based on 3-D MHD simulation results.
7. We also estimated the lower limit of instantaneous atmospheric ion escape flux due to detachment of plasma clouds during the late non-linear development of K–H instability to be $\sim 5.90 \times 10^{26}$ particles/s.
8. The 3-D MHD simulations of the event studied here demonstrates that 3-D reconnection in the vortices results in mass loss with rate of 9×10^{23} particles/s.

To the best of our knowledge, the case study of MAVEN magnetic fields and plasma observations presented here provides the first evidence for the occurrence of fully developed vortices associated with the Kelvin–Helmholtz instability near the northern polar terminator region of the Martian induced magnetosphere boundary. Although the K–H instability at Mars is phenomenologically similar to that at Earth, our analyses clearly demonstrated that there are many aspects of the instability, such as onset or stability criteria, occurrence and evolution, that is, fundamentally different at Mars due to the difference in magnetic field geometry and plasma environment (e.g., strong presence of planetary heavy ions) surrounding and within the Martian induced magnetosphere. As such, many questions regarding the nature of K–H instability at Mars (or other un-magnetized planetary bodies) remain unanswered, which includes, but not limited to, the following:

1. Are K–H vortices a common phenomenon at Mars? If so, where is the KH-unstable boundary at Mars? What IMF and solar wind conditions are most conducive for the onset and growth of K–H instability?
2. What are the particle energization processes (i.e., magnetic reconnection, secondary instabilities or other turbulent processes) occurring within or along the boundaries of the K–H vortices that allows for the loss of planetary plasma across the unstable boundary at Mars?

3. What is the global-integrated mass loss rate from the detached plasma clouds during the non-linear stage of K–H instability? How does this loss rate compared to other atmospheric loss sources?
4. What has been the role of K–H on atmospheric loss at Mars throughout the history of the solar system?

With MAVEN's continuous and simultaneous in-situ fields and particle measurements combined with state-of-the-art numerical modeling, we can now answer some of the science questions to further our physical understanding of K–H instability and its roles or contributions to the global atmospheric loss at Mars, and possibly other un-magnetized planetary bodies.

Data Availability Statement

Data sets analyzed in this study are publicly available and archived with the NASA Planetary Data System (PDS) (https://pds-ppi.igpp.ucla.edu/mission/MAVEN).

Acknowledgments
The authors would like to acknowledge Dr. James P. McFadden for his contribution to this study in providing the STATIC data. G. Poh is supported through a cooperative agreement with Center for Research and Exploration in Space Sciences and Technology II (CRESSTII) between NASA Goddard Space Flight Center and Catholic University of America under award number 80GSFC21M0002. Work by K. Nykyri and X. Ma is supported by NASA grants NNX17AI50G and 80NSSC8K1381. X. Ma is also supported by NASA grant 80NSSC18K1108. S. Xu is supported by the NASA grant NNH10CC04C to the University of Colorado and by subcontract to Space Sciences Laboratory, University of California, Berkeley. The MAVEN project is supported by NASA through the Mars Exploration Program.

References

Acuna, M. H., Connerney, J. E. P., Lin, R. P., Mitchell, D., Carlson, C. W., McFadden, J., et al. (1999). Global distribution of crustal magnetization discovered by the Mars Global Surveyor MAG/ER experiment. *Science*, *284*(5415), 790–793.

Adamson, E., Nykyri, K., & Otto, A. (2016). The Kelvin–Helmholtz instability under parker-spiral interplanetary magnetic field conditions at the magnetospheric flanks. *Advances in Space Research*, *58*(2), 218–230. https://doi.org/10.1016/j.asr.2015.09.013

Amerstorfer, U. V., Erkaev, N. V., Taubenschuss, U., & Biernat, H. K. (2010). Influence of a density increase on the evolution of the Kelvin–Helmholtz instability and vortices. *Physics of Plasmas*, *17*(7), 072901. https://doi.org/10.1063/1.3453705

Barabash, S., Fedorov, A., Lundin, R., & Sauvaud, J. A. (2007). Martian atmospheric erosion rates. *Science*, *315*(5811), 501–503. https://doi.org/10.1126/science.1134358

Bavassano Cattaneo, M. B., Marcucci, M. F., Bogdanova, Y. V., Rème, H., Dandouras, I., Kistler, L. M., & Lucek, E. (2010). Global reconnection topology as inferred from plasma observations inside Kelvin–Helmholtz vortices. *Annales Geophysicae*, *28*, 893–906. https://doi.org/10.5194/angeo-28-893-2010

Bertucci, C., Duru, F., Edberg, N., Fraenz, M., Martinecz, C., Szego, K., & Vaisberg, O. (2011). The induced magnetospheres of Mars, Venus, and Titan. *Space Science Reviews*, *162*(1–4), 113–171. https://doi.org/10.1007/978-1-4614-3290-6_5

Birn, J. (1980). Computer studies of the dynamic evolution of the geomagnetic tail. *Journal of Geophysical Research*, *85*(A3), 1214–1222. https://doi.org/10.1029/JA085iA03p01214

Boardsen, S. A., Sundberg, T., Slavin, J. A., Anderson, B. J., Korth, H., Solomon, S. C., & Blomberg, L. G. (2010). Observations of Kelvin-Helmholtz waves along the dusk-side boundary of Mercury's magnetosphere during MESSENGER's third flyby. *Geophysical Research Letters*, *37*(12). https://doi.org/10.1029/2010GL043606

Borgogno, D., Califano, F., Faganello, M., & Pegoraro, F. (2015). Double reconnected magnetic structures driven by Kelvin–Helmholtz vortices at the Earth's magnetosphere. *Physics of Plasmas*, *22*(3), 032301. https://doi.org/10.1063/1.4913578

Brace, L. H., Theis, R. F., & Hoegy, W. R. (1982). Plasma clouds above the ionopause of Venus and their implications. *Planetary and Space Science*, *30*(1), 29–37. https://doi.org/10.1016/0032-0633(82)90069-1

Brain, D. A., Lillis, R. J., Mitchell, D. L., Halekas, J. S., & Lin, R. P. (2007). Electron pitch angle distributions as indicators of magnetic field topology near Mars. *Journal of Geophysical Research*, *112*(A9). https://doi.org/10.1029/2007JA012435

Brain, D. A., McFadden, J. P., Halekas, J. S., Connerney, J. E. P., Bougher, S. W., Curry, S., et al. (2015). The spatial distribution of planetary ion fluxes near Mars observed by MAVEN. *Geophysical Research Letters*, *42*, 9142–9148. https://doi.org/10.1002/2015GL065293

Chandrasekhar, S. (1961). *Hydromagnetic and hydrodynamic stability* (p. 652). Oxford University Press.

Chong, G. S., Pope, S., Walker, S. N., Frahm, R. A., Zhang, T. L., & Futaana, Y. (2018). A statistical study of ionospheric boundary wave formation at Venus. *Journal of Geophysical Research: Space Physics*, *123*, 7668–7685. https://doi.org/10.1029/2018JA025644

Connerney, J. E. P., Espley, J. R., DiBraccio, G. A., Gruesbeck, J. R., Oliversen, R. J., Mitchell, D. L., et al. (2015). First results of the MAVEN magnetic field investigation. *Geophysical Research Letters*, *42*, 8819–8827. https://doi.org/10.1002/2015GL065366

Cowee, M. M., Winske, D., & Gary, S. P. (2009). Two-dimensional hybrid simulations of superdiffusion at the magnetopause driven by Kelvin-Helmholtz instability. *Journal of Geophysical Research*, *114*(A10). https://doi.org/10.1029/2009JA014222

Cowee, M. M., Winske, D., & Gary, S. P. (2010). Hybrid simulations of plasma transport by Kelvin-Helmholtz instability at the magnetopause: Density variations and magnetic shear. *Journal of Geophysical Research*, *115*(A6). https://doi.org/10.1029/2009JA015011

Crider, D., Cloutier, P., Law, C., Walker, P., Chen, Y., Acuña, M., et al. (2000). Evidence of electron impact ionization in the magnetic pileup boundary of Mars. *Geophysical Research Letters*, *27*(1), 45–48. https://doi.org/10.1029/1999gl003625

deHoffmann, F., & Teller, E. (1957). Magneto-hydrodynamic shocks. *Physical Review*, *80*(4), 692–703. https://doi.org/10.1103/physrev.80.692

Delamere, P. A., Wilson, R. J., Eriksson, S., & Bagenal, F. (2013). Magnetic signatures of Kelvin-Helmholtz vortices on Saturn's magnetopause: Global survey. *Journal of Geophysical Research: Space Physics*, *118*, 393–404. https://doi.org/10.1029/2012JA018197

DiBraccio, G. A., Espley, J. R., Gruesbeck, J. R., Connerney, J. E. P., Brain, D. A., Halekas, J. S., et al. (2015). Magnetotail dynamics at Mars: Initial MAVEN observations. *Geophysical Research Letters*, *42*, 8828–8837. https://doi.org/10.1002/2015GL065248

DiBraccio, G. A., Luhmann, J. G., Curry, S. M., Espley, J. R., Xu, S., Mitchell, D. L., et al. (2018). The twisted configuration of the Martian magnetotail: MAVEN observations. *Geophysical Research Letters*, *45*, 4559–4568. https://doi.org/10.1029/2018GL077251

Dubinin, E., Fraenz, M., Fedorov, A., Lundin, R., Edberg, N., Duru, F., & Vaisberg, O. (2011). Ion energization and escape on Mars and Venus. In *The plasma environment of Venus, Mars, and Titan* (Vol. 162, pp. 173–211). Springer.

Dubinin, E., Lundin, R., & Schwingenschuh, K. (1994). Solar wind electrons as tracers of the Martian magnetotail topology. *Journal of Geophysical Research*, *99*(A11), 21233–21240. https://doi.org/10.1029/94JA01271

Eastwood, J. P., & Kiehas, S. A. (2015). Origin and evolution of plasmoids and flux ropes in the magnetotails of Earth and Mars. In A. Keiling, C. M. Jackman, & P. A. Delamere (Eds.), *Magnetotails in the solar system* (pp. 269–287). John Wiley. https://doi.org/10.1002/9781118842324.ch16

Elphic, R. C., & Ershkovich, A. I. (1984). On the stability of the ionopause of Venus. *Journal of Geophysical Research*, *89*(A2), 997–1002. https://doi.org/10.1029/JA089iA02p00997

Eriksson, S., Lavraud, B., Wilder, F. D., Stawarz, J. E., Giles, B. L., Burch, J. L., et al. (2016). Magnetospheric Multiscale observations of magnetic reconnection associated with Kelvin-Helmholtz waves. *Geophysical Research Letters*, *43*, 5606–5615. https://doi.org/10.1002/2016GL068783

Espley, J. R. (2018). The Martian magnetosphere: Areas of unsettled terminology. *Journal of Geophysical Research: Space Physics*, *123*, 4521–4525. https://doi.org/10.1029/2018JA025278

Fadanelli, S., Faganello, M., Califano, F., Cerri, S. S., Pegoraro, F., & Lavraud, B. (2018). North-south asymmetric Kelvin–Helmholtz instability and induced reconnection at the Earth's magnetospheric flanks. *Journal of Geophysical Research: Space Physics*, *123*, 9340–9356. https://doi.org/10.1029/2018JA025626

Faganello, M., Califano, F., & Pegoraro, F. (2008). Competing mechanisms of plasma transport in inhomogeneous configurations with velocity shear: The solar-wind interaction with earth's magnetosphere. *Physical Review Letters*, *100*(1), 015001. https://doi.org/10.1103/physrevlett.100.015001

Faganello, M., Califano, F., Pegoraro, F., Andreussi, T., & Benkadda, S. (2012). Magnetic reconnection and Kelvin–Helmholtz instabilities at the Earth's magnetopause. *Plasma Physics and Controlled Fusion*, *54*(12), 124037. https://doi.org/10.1088/0741-3335/54/12/124037

Faganello, M., Califano, F., Pegoraro, F., & Retino, A. (2014). Kelvin–Helmholtz vortices and double mid-latitude reconnection at the Earth's magnetopause: Comparison between observations and simulations. *Europhysics Letters*, *107*(1), 19001. https://doi.org/10.1209/0295-5075/107/19001

Fairfield, D. H., Kuznetsova, M. M., Mukai, T., Nagai, T., Gombosi, T. I., & Ridley, A. J. (2007). Waves on the dusk flank boundary layer during very northward interplanetary magnetic field conditions: Observations and simulation. *Journal of Geophysical Research*, *112*(A8). https://doi.org/10.1029/2006JA012052

Fairfield, D. H., Otto, A., Mukai, T., Kokubun, S., Lepping, R. P., Steinberg, J. T., et al. (2000). Geotail observations of the Kelvin-Helmholtz instability at the equatorial magnetotail boundary for parallel northward fields. *Journal of Geophysical Research*, *105*(A9), 21159–21173. https://doi.org/10.1029/1999JA000316

Fujimoto, M., & Terasawa, T. (1994). Anomalous ion mixing within an MHD scale Kelvin-Helmholtz vortex. *Journal of Geophysical Research*, *99*(A5), 8601–8613. https://doi.org/10.1029/93JA02722

Gershman, D. J., Raines, J. M., Slavin, J. A., Zurbuchen, T. H., Sundberg, T., et al. (2015). MESSENGER observations of multiscale Kelvin–Helmholtz vortices at Mercury. *Journal of Geophysical Research: Space Physics*, *120*, 4354–4368. https://doi.org/10.1002/2014JA020903

Gruesbeck, J., Espley, J. R., Connerney, J. E., DiBraccio, G. A., Soobiah, Y. I. J., Mazelle, C. X., et al. (2016). MAVEN observations of the thickness and asymmetry of the Martian induced magnetospheric boundary. *American Geophysical Union, Fall General Assembly 2016* (pp. P13A–1885, abstract id).

Gunell, H., Amerstorfer, U. V., Nilsson, H., Grima, C., Koepke, M., Fränz, M., et al. (2008). Shear driven waves in the induced magnetosphere of Mars. *Plasma Physics and Controlled Fusion*, *50*(7), 074018. https://doi.org/10.1088/0741-3335/50/7/074018

Halekas, J. S., Brain, D. A., Ruhunusiri, S., McFadden, J. P., Mitchell, D. L., Mazelle, C., et al. (2016). Plasma clouds and snowplows: Bulk plasma escape from Mars observed by MAVEN. *Geophysical Research Letters*, *43*, 1426–1434. https://doi.org/10.1002/2016GL067752

Hasegawa, H., Fujimoto, M., Phan, T. D., Reme, H., Balogh, A., Dunlop, M. W., et al. (2004). Transport of solar wind into Earth's magnetosphere through rolled-up Kelvin–Helmholtz vortices. *Nature*, *430*(7001), 755–758. https://doi.org/10.1038/nature02799

Hasegawa, H., Fujimoto, M., Takagi, K., Saito, Y., Mukai, T., & Rème, H. (2006). Single-spacecraft detection of rolled-up Kelvin-Helmholtz vortices at the flank magnetopause. *Journal of Geophysical Research*, *111*(A9). https://doi.org/10.1029/2006JA011728

Henri, P., Cerri, S. S., Califano, F., Pegoraro, F., Rossi, C., Faganello, M., et al. (2013). Nonlinear evolution of the magnetized Kelvin–Helmholtz instability: From fluid to kinetic modeling. *Physics of Plasmas*, *20*, 102118. https://doi.org/10.1063/1.4826214

Henry, Z. W., Nykyri, K., Moore, T. W., Dimmock, A. P., & Ma, X. (2017). On the dawn-dusk asymmetry of the Kelvin-Helmholtz instability between 2007 and 2013. *Journal of Geophysical Research: Space Physics*, *122*, 11888–11900. https://doi.org/10.1002/2017JA024548

Hwang, K.-J., Kuznetsova, M. M., Sahraoui, F., Goldstein, M. L., Lee, E., & Parks, G. K. (2011). Kelvin-Helmholtz waves under southward interplanetary magnetic field. *Journal of Geophysical Research*, *116*(A8). https://doi.org/10.1029/2011JA016596

Jakosky, B. M., Brain, D., Chaffin, M., Curry, S., Deighan, J., Grebowsky, J., et al. (2018). Loss of the Martian atmosphere to space: Present-day loss rates determined from MAVEN observations and integrated loss through time. *Icarus*, *315*, 146–157.

Jakosky, B. M., Grebowsky, J. M., Luhmann, J. G., & Brain, D. A. (2015). Initial results from the MAVEN mission to Mars. *Geophysical Research Letters*, *42*, 8791–8802. https://doi.org/10.1002/2015GL065271

Kavosi, S., & Raeder, J. (2015). Ubiquity of Kelvin–Helmholtz waves at Earth's magnetopause. *Nature Communications*, *6*, 7019. https://doi.org/10.1038/ncomms8019

Khrabrov, A. V., & Sonnerup, B. U. Ö. (1998). DeHoffmann-Teller analysis. In G. Paschmann, & P. W. Daly (Eds.), *Analysis methods for multi-spacecraft data*. ISSI Scientific Report Series (Vol. SR-001, pp. 221–248).

Liljeblad, E., Sundberg, T., Karlsson, T., & Kullen, A. (2015). Statistical investigation of Kelvin-Helmholtz waves at the magnetopause of Mercury. *Journal of Geophysical Research: Space Physics*, *119*, 9670–9683. https://doi.org/10.1002/2014JA020614

Lillis, R. J., & Brain, D. A. (2013). Nightside electron precipitation at Mars: Geographic variability and dependence on solar wind conditions. *Journal of Geophysical Research: Space Physics*, *118*, 3546–3556. https://doi.org/10.1002/jgra.50171

Lin, D., Wang, C., Li, W., Tang, B., Guo, X., & Peng, Z. (2014). Properties of Kelvin-Helmholtz waves at the magnetopause under northward interplanetary magnetic field: Statistical study. *Journal of Geophysical Research: Space Physics*, *119*, 7485–7494. https://doi.org/10.1002/2014JA020379

Ma, X., Delamere, P. A., Nykyri, K., Burkholder, B., Neupane, B., & Rice, R. C. (2019). Comparison between fluid simulation with test particles and hybrid simulation for the Kelvin-Helmholtz instability. *Journal of Geophysical Research: Space Physics*, *124*, 6654–6668. https://doi.org/10.1029/2019ja026890

Ma, X., Delamere, P. A., Otto, A., & Burkholder, B. (2017). Plasma transport driven by the three-dimensional Kelvin-Helmholtz instability. *Journal of Geophysical Research: Atmospheres*, *122*, 10382–10395. https://doi.org/10.1002/2017JA024394

Masson, A., & Nykyri, K. (2018). Kelvin–Helmholtz instability: Lessons learned and ways forward. *Space Science Reviews*, *214*, 71. https://doi.org/10.1007/s11214-018-0505-6

Masters, A., Achilleos, N., Bertucci, C., Dougherty, M. K., Kanani, S. J., Arridge, C. S., et al. (2009). Surface waves on Saturn's dawn flank magnetopause driven by the Kelvin–Helmholtz instability. *Planetary and Space Science*, *57*(14–15), 1769–1778. https://doi.org/10.1016/j.pss.2009.02.010

Masters, A., Achilleos, N., Kivelson, M. G., Sergis, N., Dougherty, M. K., Thomsen, M. F., et al. (2010). Cassini observations of a Kelvin-Helmholtz vortex in Saturn's outer magnetosphere. *Journal of Geophysical Research*, *115*(A7). https://doi.org/10.1029/2010JA015351

Matsumoto, Y., & Hoshino, M. (2004). Onset of turbulence induced by a Kelvin-Helmholtz vortex. *Geophysical Research Letters*, *31*(2). https://doi.org/10.1029/2003GL018195

Matsumoto, Y., & Hoshino, M. (2006). Turbulent mixing and transport of collisionless plasmas across a stratified velocity shear layer. *Journal of Geophysical Research*, *111*(A5). https://doi.org/10.1029/2004JA010988

Matsunaga, K., Seki, K., Brain, D. A., Hara, T., Masunaga, K., Mcfadden, J. P., et al. (2017). Statistical study of relations between the induced magnetosphere, ion composition, and pressure balance boundaries around mars based on MAVEN observations. *Journal of Geophysical Research: Space Physics*, *122*, 9723–9737. https://doi.org/10.1002/2017JA024217

McFadden, J. P., Livi, R., Luhmann, J., Connerney, J., Mitchell, D., Mazelle, C., et al. (2015). Structure of the Martian ionosphere and atmospheric loss: MAVEN STATIC first results. *Lunar and Planetary Science Conference* (Vol. 1832, p. 2899).

Mitchell, D. L., Lin, R. P., Mazelle, C., Rème, H., Cloutier, P. A., Connerney, J. E. P., et al. (2001). Probing Mars' crustal magnetic field and ionosphere with the MGS Electron Reflectometer. *Journal of Geophysical Research*, *106*(E10), 23419–23427. https://doi.org/10.1029/2000JE001435

Mitchell, D. L., Mazelle, C., Sauvaud, J. A., Thocaven, J. J., Rouzaud, J., Fedorov, A., et al. (2016). The MAVEN solar wind electron analyzer. *Space Science Reviews*, *200*(1–4), 495–528. https://doi.org/10.1007/s11214-015-0232-1

Miura, A. (1982). Nonlinear evolution of the magnetohydrodynamic Kelvin–Helmholtz instability. *Physical review letters*, *49*(11), 779–782. https://doi.org/10.1103/physrevlett.49.779

Miura, A., & Pritchett, P. L. (1982). Nonlocal stability analysis of the MHD Kelvin-Helmholtz instability in a compressible plasma. *Journal of Geophysical Research*, *87*(A9), 7431–7444. https://doi.org/10.1029/ja087ia09p07431

Möstl, U. V., Erkaev, N. V., Zellinger, M., Lammer, H., Gröller, H., Biernat, H. K., & Korovinskiy, D. (2011). The Kelvin–Helmholtz instability at Venus: What is the unstable boundary? *Icarus*, *216*(2), 476–484. https://doi.org/10.1016/j.icarus.2011.09.012

Nakamura, T. K. M., & Daughton, W. (2014). Turbulent plasma transport across the Earth's low-latitude boundary layer. *Geophysical Research Letters*, *41*, 8704–8712. https://doi.org/10.1002/2014GL061952

Nakamura, T. K. M., & Fujimoto, M. (2005). Magnetic reconnection within rolled-up MHD-scale Kelvin-Helmholtz vortices: Two-fluid simulations including finite electron inertial effects. *Geophysical Research Letters*, *32*(21). https://doi.org/10.1029/2005GL023362

Nakamura, T. K. M., Hasegawa, H., Daughton, W., Eriksson, S., Li, W. Y., & Nakamura, R. (2017). Turbulent mass transfer caused by vortex induced reconnection in collisionless magnetospheric plasmas. *Nature Communications*, *8*, 1582. https://doi.org/10.1038/s41467-017-01579-0

Nakamura, T. K. M., Hasegawa, H., & Shinohara, I. (2010). Kinetic effects on the Kelvin–Helmholtz instability in ion-to-magnetohydrodynamic scale transverse velocity shear layers: Particle simulations. *Physics of Plasmas*, *17*(4), 042119. https://doi.org/10.1063/1.3385445

Nakamura, T. K. M., Hayashi, D., Fujimoto, M., & Shinohara, I. (2004). Decay of MHD-scale Kelvin–Helmholtz vortices medicated by parasitic electron dynamics. *Physical Review Letters*, *92*, 145001. https://doi.org/10.1103/physrevlett.92.145001

Nakamura, T. K. M., Plaschke, F., Hasegawa, H., Liu, Y.-H., Hwang, K.-J., Blasl, K. A., & Nakamura, R. (2020). Decay of Kelvin-Helmholtz vortices at the Earth's magnetopause under pure southward IMF conditions. *Geophysical Research Letters*, *47*, e2020GL087574. https://doi.org/10.1029/2020GL087574

Nykyri, K. (2013). Impact of MHD shock physics on magnetosheath asymmetry and Kelvin-Helmholtz instability. *Journal of Geophysical Research: Space Physics*, *118*, 5068–5081. https://doi.org/10.1002/jgra.50499

Nykyri, K., & Otto, A. (2001). Plasma transport at the magnetospheric boundary due to reconnection in Kelvin-Helmholtz vortices. *Geophysical Research Letters*, *28*, 3565–3568. https://doi.org/10.1029/2001GL013239

Nykyri, K., & Otto, A. (2004). Influence of the Hall term on KH instability and reconnection inside KH vortices. *Annales Geophysicae*, *22*, 935–949. https://doi.org/10.5194/angeo-22-935-2004

Nykyri, K., Otto, A., Lavraud, B., Mouikis, C., Kistler, L. M., Balogh, A., & Reme, H. (2006). Cluster observations of reconnection due to the Kelvin–Helmholtz instability at the dawnside magnetospheric flank. *Annales Geophysicae*, *24*(10), 2619–2643. https://doi.org/10.5194/angeo-24-2619-2006

Øieroset, M., Phan, T. D., Lin, R. P., & Sonnerup, B. U. (2000). Walén and variance analyses of high-speed flows observed by Wind in the midtail plasma sheet: Evidence for reconnection. *Journal of Geophysical Research*, *105*(A11), 25247–25263. https://doi.org/10.1029/2000JA900075

Ong, R. S. B., & Roderick, N. (1972). On the Kelvin–Helmholtz instability of the Earth's magnetopause. *Planetary and Space Science*, *20*(1). https://doi.org/10.1016/0032-0633(72)90135-3

Otto, A. (1990). 3D resistive MHD computations of magnetospheric physics. *Computer Physics Communications*, *59*, 185–195. https://doi.org/10.1016/0010-4655(90)90168-z

Otto, A., & Fairfield, D. H. (2000). Kelvin-Helmholtz instability at the magnetotail boundary: MHD simulation and comparison with Geotail observations. *Journal of Geophysical Research*, *105*(A9), 21175–21190. https://doi.org/10.1029/1999JA000312

Penz, T., Erkaev, N. V., Biernat, H. K., Lammer, H., Amerstorfer, U. V., Gunell, H., et al. (2004). Ion loss on Mars caused by the Kelvin–Helmholtz instability. *Planetary and Space Science*, *52*(13), 1157–1167. https://doi.org/10.1016/j.pss.2004.06.001

Petschek, H. E. (1964). *AAS-NASA symposium on solar flares* (p. 425). National Aeronautics and Space Administration.

Pope, S. A., Balikhin, M. A., Zhang, T. L., Fedorov, A. O., Gedalin, M., & Barabash, S. (2009). Giant vortices lead to ion escape from Venus and re-distribution of plasma in the ionosphere. *Geophysical Research Letters*, *36*(7). https://doi.org/10.1029/2008gl036977

Potter, D. (1973). *Computational physics*. John Wiley.

Ruhunusiri, S., Halekas, J. S., McFadden, J. P., Connerney, J. E. P., Espley, J. R., Harada, Y., et al. (2016). MAVEN observations of partially developed Kelvin-Helmholtz vortices at Mars. *Geophysical Research Letters*, *43*, 4763–4773. https://doi.org/10.1002/2016GL068926

Sisti, M., Faganello, M., Califano, F., & Lavraud, B. (2019). Satellite data-based 3-D simulation of Kelvin–Helmholtz instability and induced magnetic reconnection at the Earth's magnetopause. *Geophysical Research Letters*, *46*, 11597–11605. https://doi.org/10.1029/2019gl083282

Sonnerup, B. U. O., Papamastorakis, I., Paschmann, G., & Lühr, H. (1987). Magnetopause properties from AMPTE/IRM observations of the convection electric field: Method development. *Journal of Geophysical Research*, *92*(A11), 12137–12159. https://doi.org/10.1029/JA092iA11p12137

Sonnerup, B. U. Ö., Paschmann, G., & Phan, T.-D. (1995). Fluid aspects of reconnection at the magnetopause: In situ observations. In P. Song, B. Sonnerup, & M. Thomsen (Eds.), *Physics of the magnetopause* (pp. 167–180). https://doi.org/10.1029/GM090p0167

Sonnerup, B. U. O., & Scheible, M. (1998). Analysis methods for multi-spacecraft data. *ISSI Scientific Report*.

Sundberg, T., Boardsen, S. A., Slavin, J. A., Anderson, B. J., Korth, H., Zurbuchen, T. H., et al. (2012). MESSENGER orbital observations of large-amplitude Kelvin-Helmholtz waves at Mercury's magnetopause. *Journal of Geophysical Research*, *117*(A4). https://doi.org/10.1029/2011JA017268

Sundberg, T., Boardsen, S. A., Slavin, J. A., Blomberg, L. G., Cumnock, J. A., Solomon, S. C., et al. (2011). Reconstruction of propagating Kelvin–Helmholtz vortices at Mercury's magnetopause. *Planetary and Space Science*, *59*(15), 2051–2057. https://doi.org/10.1016/j.pss.2011.05.008

Sundberg, T., Boardsen, S. A., Slavin, J. A., Blomberg, L. G., & Korth, H. (2010). The Kelvin–Helmholtz instability at Mercury: An assessment. *Planetary and Space Science*, *58*(11), 1434–1441. https://doi.org/10.1016/j.pss.2010.06.008

Takagi, K., Hashimoto, C., Hasegawa, H., Fujimoto, M., & TanDokoro, R. (2006). Kelvin-Helmholtz instability in a magnetotail flank-like geometry: Three-dimensional MHD simulations. *Journal of Geophysical Research*, *111*(A8). https://doi.org/10.1029/2006JA011631

Taylor, M. G. G. T., Hasegawa, H., Lavraud, B., Phan, T., Escoubet, C. P., Dunlop, M. W., et al. (2012). Spatial distribution of rolled up Kelvin–Helmholtz vortices at Earth's dayside and flank magnetopause. *Annales Geophysicae*, *30*(6), 1025–1035. https://doi.org/10.5194/angeo-30-1025-2012

Terada, N., Machida, S., & Shinagawa, H. (2002). Global hybrid simulation of the Kelvin–Helmholtz instability at the Venus ionopause. *Journal of Geophysical Research*, *107*(A12), SMP 30-1–SMP 30-20. https://doi.org/10.1029/2001JA009224

Terasawa, T., Fujimoto, M., Karimabadi, H., & Omidi, N. (1992). Anomalous ion mixing within a Kelvin–Helmholtz vortex in a collisionless plasma. *Physical Review Letters*, *68*(18), 2778–2781. https://doi.org/10.1103/physrevlett.68.2778

Thomas, V. A., & Winske, D. (1991). Kinetic simulation of the Kelvin-Helmholtz instability at the Venus ionopause. *Geophysical Research Letters*, *18*(11), 1943–1946. https://doi.org/10.1029/91gl02552

Vernisse, Y., Lavraud, B., Faganello, M., Fadanelli, S., Sisti, M., Califano, F., et al. (2020). Latitudinal dependence of the Kelvin–Helmholtz instability and beta dependence of vortex-induced high-guide field magnetic reconnection. *Journal of Geophysical Research: Space Physics*, *125*, e2019JA027333. https://doi.org/10.1029/2019JA027333

Vignes, D., Mazelle, C., Rme, H., Acuña, M. H., Connerney, J. E. P., Lin, R. P., et al. (2000). The solar wind interaction with Mars: Locations and shapes of the bow shock and the magnetic pile-up boundary from the observations of the MAG/ER experiment onboard Mars Global Surveyor. *Geophysical Research Letters*, *27*(1), 49–52. https://doi.org/10.1029/1999GL010703

Walker, A. D. M. (1981). The Kelvin–Helmholtz instability in the low-latitude boundary layer. *Planetary and Space Science*, *29*(10), 1119–1133. https://doi.org/10.1016/0032-0633(81)90011-8

Wang, J., Xu, X., Yu, J., Ye, Y., & Ye, Y. (2020). South-north asymmetry of proton density distribution in the Martian magnetosheath. *Earth and Planetary Physics*, *4*, 32–36. https://doi.org/10.26464/epp2020003

Weber, T., Brain, D., Xu, S., Mitchell, D., Espley, J., Halekas, J., et al. (2020). The influence of interplanetary magnetic field direction on Martian crustal magnetic field topology. *Geophysical Research Letters*, *47*, e2020GL087757. https://doi.org/10.1029/2020GL087757

Winterhalter, D., Acuña, M., & Zakharov, A. (Eds.). (2004). *Mars' magnetism and its interaction with the solar wind* (Vol. 18). Springer Science & Business Media.

Wolff, R. S., Goldstein, B. E., & Yeates, C. M. (1980). The onset and development of Kelvin-Helmholtz instability at the Venus ionopause. *Journal of Geophysical Research*, *85*(A13), 7697–7707. https://doi.org/10.1029/JA085iA13p07697

Xu, S., Mitchell, D., Liemohn, M., Fang, X., Ma, Y., Luhmann, J., et al. (2017). Martian low-altitude magnetic topology deduced from MAVEN/SWEA observations. *Journal of Geophysical Research: Space Physics*, *122*, 1831–1852. https://doi.org/10.1002/2016JA023467

Xu, S., Mitchell, D. L., Mcfadden, J. P., Collinson, G., Harada, Y., Lillis, R., et al. (2018). Field-aligned potentials at Mars from MAVEN observations. *Geophysical Research Letters*, *45*, 10119–10127. https://doi.org/10.1029/2018GL080136

Xu, S., Mitchell, D. L., Weber, T., Brain, D. A., Luhmann, J. G., Dong, C., et al. (2020). Characterizing Mars's magnetotail topology with respect to the upstream interplanetary magnetic fields. *Journal of Geophysical Research: Space Physics*, *125*, e2019JA027755. https://doi.org/10.1029/2019JA027755

Xu, S., Weber, T., Mitchell, D. L., Brain, D. A., Mazelle, C., DiBraccio, G. A., & Espley, J. (2019). A technique to infer magnetic topology at Mars and its application to the terminator region. *Journal of Geophysical Research: Space Physics*, *124*, 1823–1842. https://doi.org/10.1029/2018JA026366

Yan, G. Q., Mozer, F. S., Shen, C., Chen, T., Parks, G. K., Cai, C. L., & McFadden, J. P. (2014). Kelvin-Helmholtz vortices observed by THEMIS at the duskside of the magnetopause under southward interplanetary magnetic field. *Geophysical Research Letters*, *41*, 4427–4434. https://doi.org/10.1002/2014GL060589